Master's thesis

Scattering of localized states in the active phase field crystal (aPFC) model

Submitted by

Johannes Kirchner

October 11, 2017

First examiner
Prof. Dr. Uwe Thiele

Second examiner
Dr. Svetlana Gurevich

Westfälische Wilhelms-Universität Münster
Fachbereich Physik
Institut für theoretische Physik

Contents

1 Introduction

In this thesis we consider the theoretical framework of self-propelled particles. In particular, our study analyses the active phase field crystal (aPFC) model. Self-propelled particles are a subtopic of active matter, which refers to soft matter that self-propels due to the transformation of chemical energy into mechanical energy. Examples of active matter can be found in nearly all sciences including chemistry [29, 21], biology [14] and physics [6, 32]. Examples of such systems include living matter like animals, bacteria or molecular motors, but also man-made self-propelled particles. A very recent application for self-propelled particles in medicine has been developed by researchers at the University of British Columbia. They produced carbonate based microparticles, that travel through blood in the direction of damaged tissue. This shall make it possible to deliver drugs to damaged tissue deep inside the human body [4].
Toner and Tu were the first to develop a quantitative theory for the collective motion of self-propelled particles, capable of explaining a broad range of phenomena [35]. It has been observed that self-propelled particles can crystallise at high densities [33], an effect that had not been included in the early models for self-propelled particles. Crystallisation and solidification processes themselves have been modelled by the phase field crystal (PFC) model, which was first introduced by Elder and his co-workers [15, 36] and describes microscale processes on diffusive time scales.
Menzel and Löwen introduced the active phase field crystal (aPFC) model in 2013 [25], which combines the PFC model with a polarization equation, motivated by the Toner-Tu theory, in order to describe the interplay of activity and crystallisation. The aPFC model provides a microscopic field theory and, like the PFC model, does not only allow for periodic, i.e., crystalline states, but also for localised states that represent finite-size crystals. Both resting periodic and resting localised states start to drift at a critical value of the coupling parameter v_0 between density and polarisation [26].
The localised states in the aPFC model are the main subject of this thesis. We provide an extensive description of their various forms and test their scattering behaviour. In this way, it is tested whether the aPFC model can provide the framework for a description of self-propelled particles like for example microswimmers.

We begin by introducing the Swift-Hohenberg (SH) in chapter 2 as a model equation for the transition between uniform states and periodic states. The relatively simple SH equation is also a convenient model to introduce the calculus of variation, linear stability analysis and weakly nonlinear analysis. These and

the numerical continuation tool AUTO07 will be used to determine bifurcation diagrams for uniform, periodic and localised states.
Next, we introduce the PFC model in order to describe crystallisation. After a short derivation from classical density functional theory, the PFC model is analysed in chapter 3. Differences to the SH equation, like mass conservation, but also similarities are outlined and a bifurcation diagram is presented.
Finally, the aPFC model is introduced and analysed in chapter 4. Linear stability analysis serves as a convenient tool to create a phase diagram of travelling crystals, resting crystals and the uniform state. Furthermore the drift instability from resting towards travelling states is presented.
In order to attain extensive knowledge over the localised states of the aPFC model, numerical continuation is performed in chapter 5. Interesting bifurcation behaviour is highlighted and notable features of the aPFC model are explained. Also, fold continuation proves to be an effective method to give an overview over the bifurcation behaviour.
As last step, we look into the scattering behaviour of localised states in chapter 6. By performing scattering experiments for various parameters, we show different behaviour and highlight interesting features of the aPFC model. In chapter 7, we summarize and discuss our results before suggesting what might be worth investigating in the future.

2 Swift-Hohenberg equation (SH)

One of the most important models in order to study pattern formation is the Swift-Hohenberg equation. It was first introduced to describe the Rayleigh-Bérnard convection and captures the essential properties of a system undergoing a transition from a uniform state towards a patterned state [10]. In its most general form it is given by

$$\partial_t u = ru - \left(\partial_x^2 + q_c^2\right)^2 u + f(u), \tag{2.1}$$

where $u(x,t)$ is an order parameter field in most cases related to a density, r is the control parameter, q_c the critical wavenumber and $f(u)$ stands for a nonlinearity. In the following we use

$$f(u) = b_2 u^2 - b_3 u^3 \tag{2.2}$$

as in [7], but there are numerous alternatives each exhibiting a slightly different pattern formation process [8, 30].
The examination of the SH will be divided into two parts. First the Calculus of Variation is invoked to demonstrate the importance of stationary states in the SH and then stability analysis and numerical calculations are used to analyse the stationary states.

2.1 Variational Approach

We start this section by giving a recapitulation of the calculus of variation as known from classical mechanics and then explain how the formalism can be expanded to partial differential equations. Then Euler-Lagrange equation and Hamiltonian will take a different form compared to the classical calculations, so they will be reintroduced. Finally, the general derivations will be applied to the SH equation.
The basic idea of the calculus of variation is to treat the desired solution as a minimizer of a potential, which has the property of attributing a real number to any given function. This approach is well known from Analytical Mechanics [18], where the potential takes the form of

$$V[x] = \int_{t_1}^{t_2} L(t, x(t), \dot{x}(t))\, dt, \tag{2.3}$$

where L is called the Lagrangian and depends on the time t, the trajectory x and the velocity $\dot{x}$. In order to find the minimum of the potential its functional

derivative has to be set to zero, which yields the Euler-Lagrange equation (2.4). The minimizing trajectory must fulfil the Euler-Lagrange equation, which gives us the evolution equation of the trajectory. In classical mechanics that would simply be the Newtonian equation of motion.

$$\frac{\delta V}{\delta x} = 0 \quad \Leftrightarrow \quad \frac{\partial L}{\partial x} - \frac{d}{dt}\frac{\partial L}{\partial(\partial \dot{x})} = 0 \tag{2.4}$$

As such, this approach does not work for the SH, because u is not a trajectory $x(t)$ but an order parameter field $u(x,t)$ that depends on both time and space. Furthermore the Newtonian equation of motion only has derivatives up to second order, whereas the SH has derivative up to fourth order. The variational Ansatz from classical mechanics hence has to be adjusted to work for the SH (Note that the following formalism is shown in general and does not only apply to the SH). We initially limit our description to equilibrium solutions and introduce the potential

$$V[u] = \int_\Omega L(x, u(x,t), \partial_x u(x,t), \partial_x^2 u(x,t), \dots, \partial_x^n u(x,t))\, dx, \tag{2.5}$$

whose Lagrangian depends on arbitrarily high spatial derivatives and has no explicit time dependence. The time-independent minimizers $u(x)$ of the potential give us the equilibria and in order to obtain the evolution equation close to equilibrium we set

$$\partial_t u = -\frac{\delta V}{\delta u}. \tag{2.6}$$

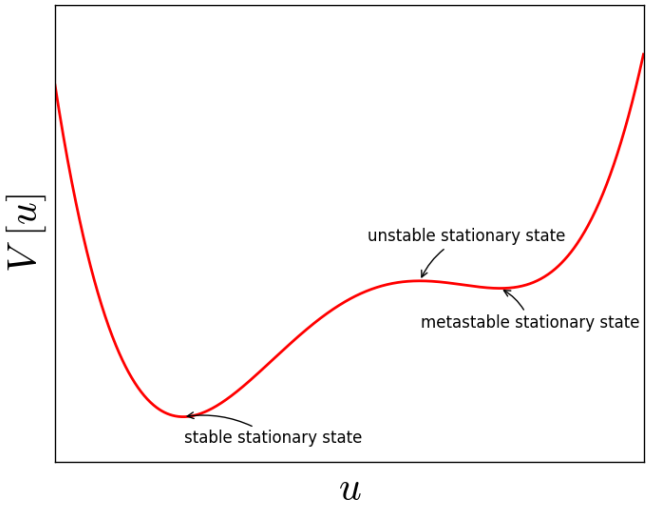

Figure 2.1: The potential $V[u]$ for various densities u. Minima and Maxima are associated with stable and unstable stationary states, respectively. It should be noted that the potential V is not a continuous function of u, so the figure is to be taken qualitatively.

It will be shown in section 2.1.2, that the potential always decreases over time under suitable boundary conditions. This implies that the system always approaches equilibrium and the temporal evolution close to equilibrium is given by Eq. (2.6). The (local) minimizers (or indeed maximizers) of $V[u]$ are called stationary states. Maximizers represent unstable stationary states, local minimizers metastable stationary states and the global minimizer a stable stationary state (see Fig. 2.1).

2.1.1 Euler-Lagrange equation

In the following it will be shown how a functional derivative is calculated in general. We will explicitly show how Euler-Lagrange equations look like for Lagrangians that may depend on second or higher order derivatives. The functional derivative is commonly defined by the help of an arbitrary smooth function $\varphi \in C_0^\infty$ with compact support. This means that φ vanishes at the boundaries, which is necessary as will be shown in the following calculation.

$$\int_\Omega \frac{\delta V}{\delta u}\varphi dx = \lim_{\epsilon\to 0}\frac{V(u+\epsilon\varphi)-V(u)}{\epsilon} \tag{2.7}$$

$$= \lim_{\epsilon\to 0}\frac{1}{\epsilon}\int_\Omega (L(x,u+\epsilon\varphi,\dots,\partial_x^n u+\epsilon\partial_x^n\varphi)-L(x,u,\dots,\partial_x^n u)dx \tag{2.8}$$

$$= \lim_{\epsilon\to 0}\frac{1}{\epsilon}\int_\Omega \left(\sum_{i=0}^{n}\epsilon\partial_x^i\varphi\frac{\partial L(x,u,\dots,\partial_x^n u)}{\partial(\partial_x^i u)}+\mathcal{O}(\epsilon^2)\right)dx \tag{2.9}$$

$$= \int_\Omega \left(\sum_{i=0}^{n}(-\partial_x)^i\frac{\partial L(x,u,\dots,\partial_x^n u)}{\partial(\partial_x^i u)}\right)\varphi dx + \lim_{\epsilon\to 0}\mathcal{O}(\epsilon) \tag{2.10}$$

By comparing equations (2.7) and (2.10) we can identify the functional derivative as

$$\frac{\delta V}{\delta u} = \sum_{i=0}^{n}(-\partial_x)^i\frac{\partial L}{\partial(\partial_x^i u)}. \tag{2.11}$$

For a more rigorous derivation see Ref. [11]. The Euler-Lagrange equations are found by setting the functional derivative of the potential to zero, hence equation (2.12) is the generalized version of the Euler-Lagrange equation.

$$\sum_{i=0}^{n}(-\partial_x)^i\frac{\partial L}{\partial(\partial_x^i u)} = 0 \tag{2.12}$$

For $n = 1$ this simplifies to

$$\frac{\partial L}{\partial u} - \partial_x\frac{\partial L}{\partial(\partial_x u)} = 0, \tag{2.13}$$

which is indeed in agreement with the Euler-Lagrange equation known from classical mechanics as in Eq. (2.4). The evolution equation for the order parameter field $u(x,t)$ is then obtained by setting the generalized Euler-Lagrange

equation equal to the negative temporal partial derivative of u (see Eq. 2.6).

$$\partial_t u = -\sum_{i=0}^{n} (-\partial_x)^i \frac{\partial L}{\partial(\partial_x^i u)} \tag{2.14}$$

The variational approach only works if it is possible to find a Lagrangian, such that Eq. (2.14) reproduces the desired evolution equation. This is not always the case but works for the Swift-Hohenberg equation.

2.1.2 Temporal behaviour

The whole concept of potentials is only meaningful if the potential decreases over time and the system in question hence approaches a stationary state. In the following we calculate the temporal derivative of the potential V.

$$\frac{dV}{dt} = \int_\Omega \sum_{i=0}^{n} \frac{\partial L}{\partial(\partial_x^i u)} \partial_x^i (\partial_t u) dx \tag{2.15}$$

$$= \int_\Omega \left(\sum_{i=0}^{n} (-\partial_x)^i \frac{\partial L}{\partial(\partial_x^i u)} \right) \partial_t u \; dx \tag{2.16}$$

$$= \int_\Omega \frac{\delta V}{\delta u} \partial_t u \; dx \tag{2.17}$$

$$= -\int_\Omega (\partial_t u)^2 \; dx \tag{2.18}$$

$$\leq 0 \tag{2.19}$$

Note that the partial integration from Eq. (2.15) to (2.16) only works if the system has periodic boundary conditions or goes to zero at the boundaries. If so we only have to recognize the Euler-Lagrange equation in (2.16) and replace it with the functional derivative of V to find that the potential indeed decreases over time. This is a very powerful insight, since it implies that every system with a potential and suitable boundary conditions will eventually evolve into a stationary state. This applies also to the SH and reinforces the great importance of its stationary states.

2.1.3 Hamiltonian

The Hamiltonian is well known from classical mechanics as a conserved quantity over time. Our potential is an integral over space though (Eq. 2.5), not an integral over time as known from classical mechanics (Eq. 2.3). Keeping in mind that our formalism applies to stationary states it makes therefore more sense to define a Hamiltonian which is uniform in space. The basic principle of finding canonical coordinates and then performing a Legendre transformation on the Lagrangrian is still the same [18]. A further complication to the mechanical formalism is the Lagrangian dependence of higher order derivatives. This makes it necessary to introduce as many coordinates as the highest order

derivative, so for a Lagrangian that depends up to the n-th order as in Eq. (2.5) we need n coordinates.
Adequate canonical coordinates q_i and p_i can be found by using the Ostrogradski formalism [12]. This is done by setting

$$q_i = \partial_x^{i-1} u \quad \forall i \in \{1, \dots, n\}, \tag{2.20}$$

which has the very useful property of $\partial_x q_i = q_{i+1} \quad \forall i \in \{1, \dots, n-1\}$. This is a significant simplification since the Lagrangian now depends only on the coordinates itself and the spatial derivative of q_n. As next step we perform a Legendre transformation on the Lagrangian and get

$$H = \sum_{i=1}^{n} p_i \partial_x q_i - L(q_1, \dots, q_n, \partial_x q_n). \tag{2.21}$$

The conjugate momenta p_i are not yet defined but will later be chosen such that the Hamiltonian is uniform over space. We therefore calculate the spatial partial derivative of the Hamiltonian and order it in terms of $\partial_x q_i$.

$$\partial_x H = \sum_{i=1}^{n} \left[\partial_x p_i \partial_x q_i + p_i \partial_x^2 q_i - \frac{\partial L}{\partial q_i} \partial_x q_i \right] - \frac{\partial L}{\partial(\partial_x q_n)} \partial_x^2 q_n \tag{2.22}$$

$$= \sum_{i=1}^{n} \left[\left(\partial_x p_i - \frac{\partial L}{\partial q_i} \right) \partial_x q_i \right] + \sum_{i=2}^{n} \left[p_{i-1} \partial_x q_i \right] \tag{2.23}$$

$$+ \left(p_n - \frac{\partial L}{\partial(\partial_x q_n)} \right) \partial_x^2 q_n$$

$$= \left(\partial_x p_1 - \frac{\partial L}{\partial q_1} \right) \partial_x q_1 + \sum_{i=2}^{n} \left[\left(\partial_x p_i + p_{i-1} - \frac{\partial L}{\partial q_i} \right) \partial_x q_i \right] \tag{2.24}$$

$$+ \left(p_n - \frac{\partial L}{\partial(\partial_x q_n)} \right) \partial_x^2 q_n$$

With the goal of setting Eq. (2.24) to zero, we can choose the conjugate momenta p_i in a recursive manner:

$$p_n = \frac{\partial L}{\partial(\partial_x^n u)} \tag{2.25}$$

$$p_{n-1} = \frac{\partial L}{\partial(\partial_x^{(n-1)} u)} - \partial_x \frac{\partial L}{\partial(\partial_x^n u)} \tag{2.26}$$

$$p_{n-2} = \frac{\partial L}{\partial(\partial_x^{(n-2)} u)} - \partial_x \frac{\partial L}{\partial(\partial_x^{(n-1)} u)} + \partial_x^2 \frac{\partial L}{\partial(\partial_x^n u)} \tag{2.27}$$

$$\dots$$

$$p_1 = \sum_{i=1}^{n} (-\partial_x)^{(i-1)} \frac{\partial L}{\partial(\partial_x^i u)} \tag{2.28}$$

By these choices all but the first term of Eq. (2.24) immediately vanish and we can formulate a general definition of the conjugate momenta, which is

$$p_i = \sum_{j=i}^{n} (-\partial_x)^{(j-i)} \frac{\partial L}{\partial(\partial_x^j u)}. \tag{2.29}$$

We only have to deal with the first term of Eq. (2.24), but this one is implicitly already taken care of since

$$\left(\partial_x p_1 - \frac{\partial L}{\partial q_1}\right)\partial_x q_1 = \left(-\sum_{i=1}^{n}(-\partial_x)^i \frac{\partial L}{\partial(\partial_x^i u)} - \frac{\partial L}{\partial u}\right)\partial_x u \tag{2.30}$$

$$\overset{(2.14}{=} \partial_t u\, \partial_x u. \tag{2.31}$$

Our formalism deals with stationary states, so $\partial_t u = 0$ and therefore Eq. (2.29) gives indeed the appropriate conjugate momenta such that the Hamiltonian is uniform over space. As a matter of fact, the Ostrogradski formalism is also in agreement with classical mechanics, since the conjugate momentum for $n = 1$ is simply

$$p_1 = \frac{\partial L}{\partial(\partial_x u)}, \tag{2.32}$$

which is exactly what is defined as conjugate momentum in classical mechanics [18].
Finally, the Hamiltonian gives us an analytical tool to check or even possibly derive whether a given state is indeed a stationary solution of the evolution equation in question.

2.1.4 Swift-Hohenberg

The generally derived results can now be applied to the Swift-Hohenberg equation. According to Eq. (2.14) its Lagrangian needs to fulfil

$$\partial_t u = -\sum_{i=0}^{2}(-\partial_x)^i \frac{\partial L}{\partial(\partial_x^i u)} \tag{2.33}$$

$$\Leftrightarrow ru - \left(\partial_x^2 + q_c^2\right)^2 u + f(u) = \frac{\partial L}{\partial u} - \partial_x \frac{\partial L}{\partial(\partial_x u)} + \partial_x^2 \frac{\partial L}{\partial(\partial_x^2 u)}. \tag{2.34}$$

From this a suitable Lagrangian can be constructed by comparing the left and right hand side of Eq. (2.34):

$$L = \frac{1}{2}(\partial_x^2 u)^2 - q_c^2(\partial_x u)^2 - \frac{1}{2}(r - q_c^4)u^2 - F(u) \tag{2.35}$$

$F(u)$ stands for the integral of $f(u)$, so for the nonlinearity chosen in this thesis (Eq. 2.2) the full potential is

$$V[u] = \int_\Omega \left[\frac{1}{2}(\partial_x^2 u)^2 - q_c^2(\partial_x u)^2 - \frac{1}{2}(r - q_c^4)u^2 - \frac{b_2}{3}u^3 - \frac{b_3}{4}u^4\right] dx. \tag{2.36}$$

In order to find the Hamiltonian of the SH we construct the canonical coordinates according to Eq. 2.20 and Eq. 2.29.

$$q_1 = u \qquad p_1 = -2q_c^2\partial_x u - \partial_x^3 u \tag{2.37}$$

$$q_2 = \partial_x u \qquad p_2 = \partial_x^2 u \tag{2.38}$$

Finally, the resulting Hamiltonian as a uniform quantity over space for stationary states is

$$H = p_1 \partial_x q_1 + p_2 \partial_x q_2 - L \tag{2.39}$$

$$= -q_c^2 (\partial_x u)^2 - \partial_x u \partial_x^3 u + \frac{1}{2}(\partial_x^2 u)^2 + \frac{1}{2}(r - q_c^4)u^2 + \frac{b_2}{3}u^3 + \frac{b_3}{4}u^4. \tag{2.40}$$

This result is in agreement with the Hamiltonian in the paper of Burke and Knobloch [8], where it was presented but not derived. The Hamiltonian gives us the opportunity to check for the accuracy of stationary states that were obtained numerically or in general by using approximations. If the Hamiltonian of Eq. (2.40) is not uniform over space for that state, we know that there was an error in the calculations.

2.2 Stationary States

The former section has shown the importance of stationary states, because the Swift-Hohenberg equation with periodic boundary conditions (Eq. 2.41) always evolves towards them.

$$\partial_t u = ru - \left(\partial_x^2 + q_c^2\right)^2 u + b_2 u^2 - u^3, \qquad u(x) = u(x + L) \tag{2.41}$$

In the following, those stationary states are being analysed both analytically and numerically, whereby the analysis and parameter choice ($b_2 = 0.41$, $q_c = 0.5$ and b_3 scaled to unity) follows the paper of Burke and Knobloch from 2006 [7].

2.2.1 Homogeneous Solutions

As a starting point we look at the simplest stationary states of Eq. (2.41), which are spatially homogeneous solutions where $u(t, x) = u$. The evolution equation reduces to a cubic equation that has the three solutions u_0, u_+ and u_-.

$$u_0 = 0, \quad u_\pm = \frac{b_2}{2} \pm \sqrt{\frac{b_2^2}{4} + r - q_c^4} \tag{2.42}$$

Apparently, there is a saddle-node bifurcation at $r_{bif} = \frac{b_2^2}{4} - q_c^4$, where u_+ and u_- come into existence. Next, we check the stability of the homogeneous states by using a linear stability analysis.

2.2.2 Linear Stability Analysis

The linear stability of a stationary state $u_s(x)$ is determined by analysing how an infinitesimal small perturbation $\epsilon\tilde{u}(x, t)$ behaves. We therefore take the Ansatz

$$u(x, t) = u_s(x) + \epsilon\tilde{u}(x, t) \tag{2.43}$$

with ϵ as a smallness parameter and $\tilde{u}(x,t) \sim e^{\sigma t + iqx}$, i.e. we perform both, a Fourier and Laplace transformation, of a general perturbation. After introducing (2.43) into the SH equation (2.41) we get

$$\partial_t \tilde{u}(x,t) = \mathcal{L}\left[u_s(x)\right]\tilde{u}(x,t) + \mathcal{O}(\epsilon) \tag{2.44}$$

$$\Leftrightarrow \quad \sigma\tilde{u}(x,t) = \left[r - \left(q_c^2 - q^2\right)^2 + 2b_2 u_s(x) - 3u_s^2(x)\right]\tilde{u}(x,t) \tag{2.45}$$

$$\Leftrightarrow \quad \sigma = r - \left(q_c^2 - q^2\right)^2 + 2b_2 u_s(x) - 3u_s^2(x). \tag{2.46}$$

Like the original solution, $\tilde{u}(x)$ shall also satisfy periodic boundary conditions.

$$\tilde{u}(x+L) = \tilde{u}(x) \quad \Leftrightarrow \quad L = \frac{2\pi}{q} \tag{2.47}$$

$u_s(x)$ is linearly stable if $\tilde{u}(x,t)$ is decaying, meaning that $\mathrm{Re}(\sigma) < 0$, and unstable for $\mathrm{Re}(\sigma) > 0$, in which case the perturbations grow. We therefore treat σ as a function of q with r as the control parameter. $\sigma(q)$ is called the dispersion relation and in the following we will calculate the dispersion relation for u_0, u_+ and u_-.

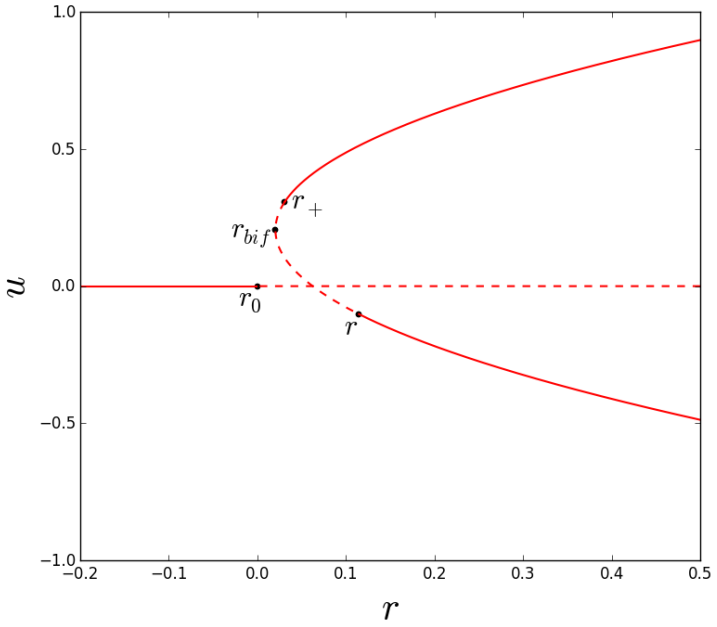

Figure 2.2: All homogeneous solutions with their stability indicated by either a dotted line (unstable) or a straight line (stable). u_+ and u_- come into existence at $r_{bif} \approx 0.02048$ and there are stability changes at $r_0 = 0$, $r_+ \approx 0.03085$ and $r_- \approx 0.11463$, respectively. Note that the stability analysis has only been performed for temporal eigenvalues and does not include the spatial eigenvalues of Eq. (2.41), which is why both solutions can be unstable at the saddle-node bifurcation.

Dispersion relation of u_0

$$\sigma(q) = r - \left(q_c^2 - q^2\right)^2 + 2b_2u_0 - 3u_0^2 \tag{2.48}$$
$$= r - (q_c^2 - q^2)^2 \tag{2.49}$$

σ is always negative for $r < 0$, meaning that u_0 is linearly stable in that regime. As r exceeds $r_0 = 0$, σ becomes positive for some wavenumbers q centered around q_c. In that case spatially periodic perturbations develop and u_0 is unstable. u_0 as a function of r with stability indicated is shown in Fig. 2.2 and the dispersion relation of u_0 is plotted in Fig. 2.3.

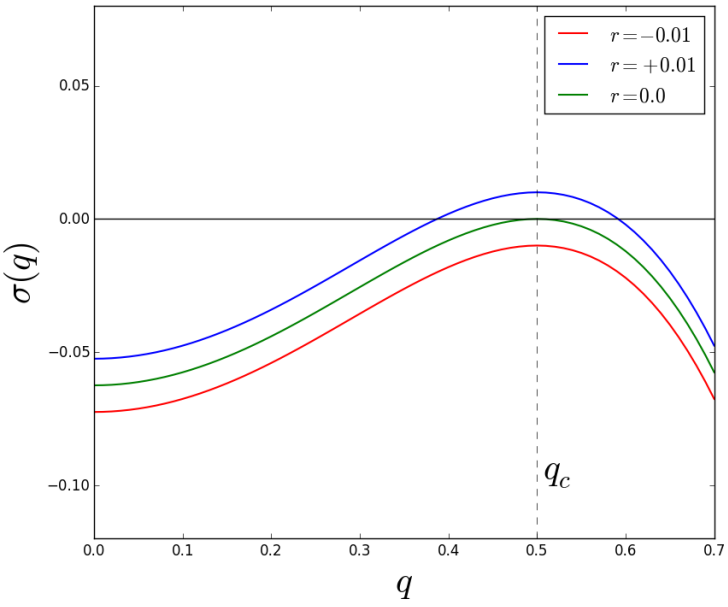

Figure 2.3: Dispersion relation of u_0 plotted for different r. The critical wavenumber $q_c = 0.5$ is marked by the dashed line.

Dispersion relation of $u_\pm$

$$\sigma(q) = r - \left(q_c^2 - q^2\right)^2 + 2b_2u_\pm - 3u_\pm^2 \tag{2.50}$$
$$= -2r - \left(q_c^2 - q^2\right)^2 + 3q_c^4 - \frac{b_2}{2}\left(b_2 \pm \sqrt{b_2^2 + 4(r - q_c^4)}\right) \tag{2.51}$$

The branches are both initially unstable at the bifurcation point r_{bif}, but both gain linear stability later. For u_+ that occurs at $r_+ \approx 0.03085$ and for u_- at $r_- \approx 0.114628$. Both branches and their region of stability are shown in Figure 2.2.

2.2.3 Weakly Nonlinear Analysis

Linear stability analysis only tells us when the homogeneous states get unstable towards periodic perturbations but not how those instabilities evolve or whether they saturate towards a stationary state. To investigate such behaviour one needs to take into account the nonlinearity of the Swift-Hohenberg equation and hence perform a weakly nonlinear analysis. The basic idea of the latter is to expand $u(x,t)$ in smallness parameters ϵ around the control parameter r_c where instabilities occur for the first time. Those perturbations are then treated as a product of the critical mode obtained from linear stability analysis and a a slow modulation.

$$e^{iqx} = e^{iq_c x} e^{i(q-q_c)x} \tag{2.52}$$

Note that $q - q_c$ in Eq. (2.52) is very small close to the bifurcation and is hence treated as a modulation of the critical mode. The goal of weakly nonlinear analysis is then to find an evolution equation for that modulation.
We carry out the analysis for the flat homogeneous solution u_0, which loses its stability at $r_0 = 0$ (see Fig. 2.3). We therefore introduce $r = \epsilon^2 \tilde{r}$, where the scaling with ϵ^2 instead of ϵ is more convenient and motivated by the outcome. A Taylor expansion of the dispersion relation around the critical control parameter r_0 and the critical wavenumber q_c leads to

$$\sigma(r,q) \approx \sigma(0,q_c) + \left(r\frac{\partial}{\partial r} + (q-q_c)\frac{\partial}{\partial q} \right) \sigma(0,q_c) \tag{2.53}$$

$$+ \frac{1}{2}\left(r^2 \frac{\partial^2}{\partial r^2} + 2r(q-q_c)\frac{\partial^2}{\partial q \partial r} + (q-q_c)^2 \frac{\partial^2}{\partial q^2} \right) \sigma(0,q_c) \tag{2.54}$$

$$= \epsilon^2 \tilde{r} - 4q_c^2 (q-q_c)^2 \tag{2.55}$$

As mentioned before the modulation is very slow, which motivates the introduction of a slow length scale X and a slow time scale T. Eq. (2.55) tells us the width of the few surviving modes which is $|q - q_c| \sim \epsilon$. Therefore the typical length of the slow modulation is

$$\frac{1}{|q-q_c|} \sim \frac{1}{\epsilon} \tag{2.56}$$

and we introduces the slow length scale $X(x) = \epsilon\, x$. Eq. (2.55) also gives us the typical time of the slow modulation

$$\frac{1}{|\sigma|} \sim \frac{1}{\epsilon^2}, \tag{2.57}$$

which motivates the introduction of the slow time scale $T(t) = \epsilon^2\, t$. We now have introduced new scales for the amplitude and can finally expand u itself.

$$u(x,t) = \epsilon u_0(x,t) + \epsilon^2 u_1(x.t) + \epsilon^3 u_2(x,t) \tag{2.58}$$

with

$$u_i(x,t) = A_i(X,T) B_i(x) \tag{2.59}$$

$u_i(x,t)$ describes the modulation of a stationary pattern on a slow time and length-scale. Plugged into the original equation (Eq. 2.41) and separated in terms of ϵ yields in first order

$$\mathcal{O}(\epsilon): \quad A_0(q_c^4 B_0 + 2q_c^2 \partial_x^2 B_0 + \partial_x^4 B_0) = 0. \tag{2.60}$$

Apparently B_0 needs to be set to $e^{iq_c x}$ and

$$u_0(x) = A_0(X,T)e^{iq_c x} + c.c. \tag{2.61}$$

where the complex conjugate is added to ensure that u is real. This tells us nothing about A_0 though and we have to check for higher orders of ϵ. In second order we get

$$\mathcal{O}(\epsilon^2): \quad A_1(q_c^4 B_1 + 2q_c^2 \partial_x^2 B_1 + \partial_x^4 B_1) = b_2(A_0 e^{iq_c x} + A_0^* e^{-iq_c x})^2. \tag{2.62}$$

Due to the square on the right hand side of Eq. (2.62) there are now different patterns on the fast spatial scale and our Ansatz needs to include a uniform pattern and one with $2q_c x$.

$$u_1(x) = A_{10}(X,T) + (A_{11}(X,T)e^{iq_c x} + A_{12}(X,T)e^{2iq_c x} + c.c.) \tag{2.63}$$

After introducing this new approach in Eq. (2.41) this yields

$$\mathcal{O}(\epsilon^2): \quad q_c^4(A_{10} + 9A_{12}e^{2iq_c x} + 9A_{12}^* e^{-2iq_c x}) = b_2(A_0 e^{iq_c x} + A_0^* e^{-iq_c x})^2 \tag{2.64}$$

in second order, which is solved by

$$A_{10} = \frac{2b_2}{q_c^4}|A_0|^2, \quad A_{12} = \frac{b_2}{9q_c^4}A_0^2. \tag{2.65}$$

We still don't have an evolution equation for A_0 though, so we have to turn to the third order of ϵ. It turns out that in order of $q_c x$ we find

$$\mathcal{O}(\epsilon^3, q_c x): \quad \partial_T A_0 - \tilde{r}A_0 - 4q_c^2 \partial_{XX} A_0 + \frac{27q_c^4 - 38b_2^2}{9q_c^4}|A_0|^2 A_0. \tag{2.66}$$

This finally gives us the equation of motion for the leading amplitude, which is

$$\partial_T A_0 = \tilde{r}A_0 + 4q_c^2 \partial_{XX} A_0 - \mu|A_0|^2 A_0 \tag{2.67}$$

with $\mu = \frac{27q_c^4 - 38b_2^2}{9q_c^4}$. Eq. (2.67) is the Ginzburg-Landau approximation of the Swift-Hohenberg equation, valid only close to the bifurcation parameter. Its simplest solution is the uniform

$$A_0(X) = \sqrt{\frac{\tilde{r}}{\mu}}e^{i\phi} \tag{2.68}$$

with a phase ϕ. When looking at the full solution of $u(x,t)$, this corresponds to spatially periodic states

$$u_p(x) = 2\sqrt{\frac{r}{\mu}}\cos(q_c x + \phi). \tag{2.69}$$

A spatially dependent solution for A_0 that fulfils the periodic boundary conditions is

$$A_0(X) = \sqrt{\frac{2\tilde{r}}{\mu}} \operatorname{sech}\left(\frac{X\sqrt{-\tilde{r}}}{2q_c}\right) e^{i\phi}, \tag{2.70}$$

which when plugged into Eq. (2.63) corresponds to localised solutions

$$u_l(x) = 2\sqrt{\frac{2r}{\mu}} \operatorname{sech}\left(\frac{x\sqrt{-r}}{2q_c}\right) \cos(q_c x + \phi). \tag{2.71}$$

The periodic state u_p and localised state u_l have been also numerically continued over a broader domain using the numerical continuation tool AUTO07 (see Fig. 2.4) [2]. The periodic branch exist only for negative r close to the bifurcation point r_0, in agreement with the analytical result. Far away from r_0 it switches direction and ultimately runs into r_+.

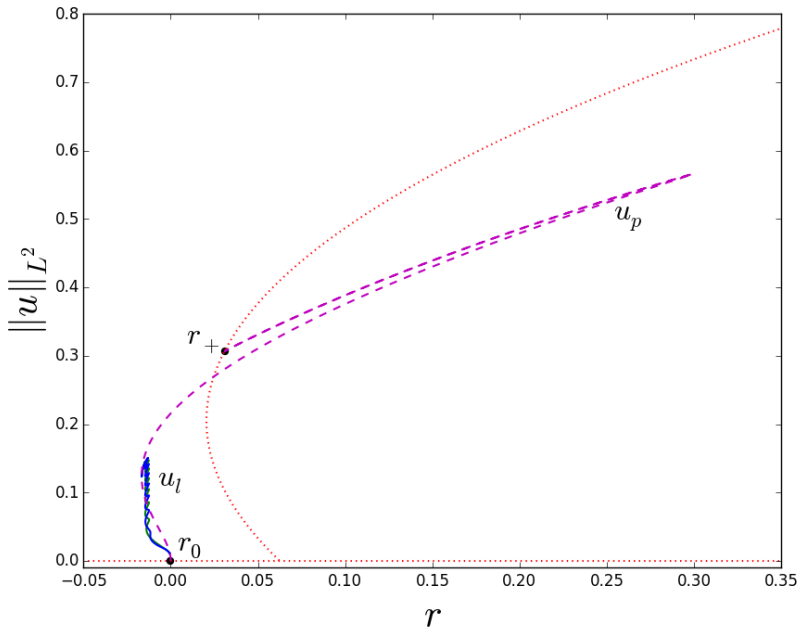

Figure 2.4: Both the periodic solution u_p (dashed margenta line) and the localised solution u_l (blue and green lines) branch off from the flat solution (red dotted lines) at the bifurcation point r_0.

u_l undergoes both for even $\phi = n\pi$ and odd $\phi = \frac{\pi}{2} + n\pi$ numerous saddle-node bifurcations (see Fig. 2.5). By doing so it increases the number of bumps until the localised state is stretched over the whole domain and runs into the periodic state. This is a characteristic feature of the Swift-Hohenberg equation called snaking [7]. It is important to mention, that the analytical result 2.71 is only true for $L \to \infty$. That is not fulfilled on a finite size domain, which is why the localised states in Fig. 2.5 branch off the periodic state as a secondary bifurcation.

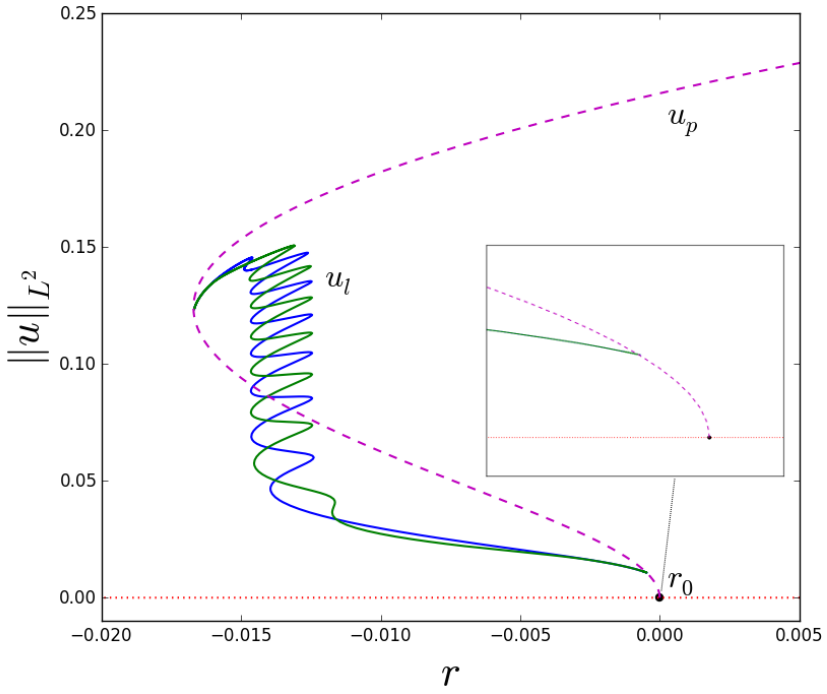

Figure 2.5: The localised solutions u_l undergo numerous saddle-node bifurcations, thereby adding more bumps and raising its L2-Norm before reaching the periodic solution u_p (dashed margenta line). The even solution $\phi = n\pi$ is depicted in green, the odd solution $\phi = \frac{\pi}{2} + n\pi$ in blue and the flat solution in red.

3 Phase field crystal (PFC) model

The PFC model is typically derived from density functional theory and provides a microscopic model of phase transitions. It is especially useful for describing the freezing transition, a transition from a uniform state towards spatially periodic states. This corresponds to a liquid transforming into a crystalline solid [16, 36].
The first section will show how the PFC model can be obtained from classical density functional theory and the second section will show its equivalency with the conserved Swift-Hohenberg (cSH) equation. Furthermore, some basic properties of the cSH and its stationary states will be presented.

3.1 Derivation from classical density functional theory

3.1.1 Classical density functional theory (cDFT)

Density functional theory is well known in the context of quantum physics, where it is used to determine the electronic structure of atoms and molecules. It was introduced by Kohn (who won the Nobel Prize in chemistry 1998 for his contributions [3]) and his co-workers Sham and Hohenberg (the same after whom the Swift-Hohenberg equation is named). It has been shown however that the approach also works for a classical setting [27].
The basic idea is to find a an equilibrium one-particle density $\rho(r)$ that minimizes the grand canonical free-energy potential Ω [16].

$$\rho(r) = \left\langle \sum_{i=1}^{N} \delta(r - r_i) \right\rangle \tag{3.1}$$

N denotes the total number of particles, and $\langle \cdot \rangle$ indicates that the average is taken. The grand canonical free-energy potential Ω depends on density ρ, chemical potential μ and temperature T, but can also be expressed in terms of the Helmholtz free-energy $\mathcal{F}$ by performing a Legendre transformation.

$$\Omega[T, \mu, \rho] = \mathcal{F}[T, \rho] - \mu \int dr\, \rho(r) \tag{3.2}$$

The Helmholtz free-energy can be decomposed in two components, the ideal gas free-energy functional $\mathcal{F}_{id}$ and the excess free-energy functional $\mathcal{F}_{exc}$ [20].

$$\mathcal{F}[T, \rho] = \mathcal{F}_{id}[T, \rho] + \mathcal{F}_{exc}[T, \rho] \tag{3.3}$$

$\mathcal{F}_{id}$ corresponds to an ideal non-interacting gas or liquid and can be solved exactly by invoking statistical mechanics [19].

$$\mathcal{F}_{id}[T,\rho] = k_B T \int dr\, \rho(r)(\ln(\Lambda^3\rho(r)) - 1) \tag{3.4}$$

k_B is the Boltzmann constant and Λ the thermal de Broglie wavelength. In order to include pair correlations, there is an additional contribution to the free-energy called excess free-energy, which is generally not exactly known. We introduce a reference density $\overline{\rho}$ and consider the derivations

$$\Delta\rho(r) = \rho(r) - \overline{\rho}. \tag{3.5}$$

Then we perform a Taylor expansion around $\Delta\rho$, where the order of the expansion corresponds to the number of interacting particles.

$$\mathcal{F}_{exc}[T,\rho] = \mathcal{F}^{(0)}_{exc}[T,\overline{\rho}] + \sum_{n=1}^{\infty} \int \prod_{i=1}^{n} dr_i \, \frac{1}{n!} \frac{\delta^n \mathcal{F}_{exc}}{\delta\rho(r_1)...\,\delta\rho(r_n)}\bigg|_{\overline{\rho}} \Delta\rho(r_i) \tag{3.6}$$

We only consider pair correlation and hence keep only the second order term and the constant contribution. Furthermore we make the assumption that the pair correlation only depends on the relative distance of the particles and end up with

$$\mathcal{F}_{exc}[T,\rho] = \mathcal{F}^{(0)}_{exc}[T,\overline{\rho}] - \frac{k_B T}{2} \int dr_1 \int dr_2\, c(r_1 - r_2)\Delta\rho(r_1)\Delta\rho(r_2), \tag{3.7}$$

where the functional derivative has been replaced with the correlation function

$$c(r_1 - r_2) = -\frac{1}{k_B T} \frac{\delta^2 \mathcal{F}_{exc}}{\delta\rho(r_1)\delta\rho(r_2)}. \tag{3.8}$$

This approximation is called the Ramakrishanan-Yusouff theory [31]. For the sake of completeness one should mention that there is typically a further contribution due to an external potential in cDFT. But since that is neglected in deriving the PFC model, it is not discussed here.

3.1.2 Derivation of the phase field crystal (PFC) model

cDFT provides a microscopic description of a fluid that is still very general. In order to describe the transition from a uniform state to a crystalline state further simplifications need to be made. As derived in [16] three assumptions are necessary to end up with the PFC model, the simplest description that is still capable of describing the phase transition. We are going to present these assumptions.

1.) Introducing an order parameter field

The first step is to replace the density ρ with an order parameter field u that is centered around the reference density $\overline{\rho}$.

$$\rho(r) = \overline{\rho}\,(1 + u(r)) \tag{3.9}$$

2.) Smallness of parameter order field

Next we assume that the order parameter field is very small and perform a Taylor expansion on the ideal free-energy functional (Eq. 3.4).

$$\mathcal{F}_{id}[T,u] = \mathcal{F}_{id}^{(0)}[T] + \overline{\rho} k_B T \int dr \left(u + \frac{u^2}{2} - \frac{u^3}{6} + \frac{u^4}{12} \right) \tag{3.10}$$

We keep only terms up to the fourth order, which is the lowest order that still enables the formation of crystalline phases.

3.) Symmetry of interaction

When dealing with spherical particles it is natural to assume that the interaction only depends on the distance $|r_1 - r_2|$ and to assume translational and spherical invariance. Plugged in the excess free-energy integral (Eq. 3.7) one can perform a gradient expansion of the correlation function, where the odd derivatives vanish due to symmetry.

$$c(r) = c_0 - c_2 \nabla_r^2 + c_4 \nabla_r^4 \tag{3.11}$$

c_0, c_2 and c_4 are constants. Finally, after excessive rescaling we end up with a free-energy functional, which depends on derivatives of second and fourth order as well as polynomial of fourth order [16].

$$\mathcal{F}[u] = \int dr \left(\frac{u}{2} \left(\beta + (q_c^2 + \nabla_r^2)^2 \right) u + \frac{u^4}{4} \right) \tag{3.12}$$

This is the expression for the free-energy commonly related to the PFC model. The corresponding order parameter equations will be discussed in the next section. Also note that the control parameter in Eq. (3.12) is called β and not r to avoid confusion with the spatial coordinates. In the following we only deal with the PFC model in one dimension so r is going to be replaced by x and β by r. Also the free-energy functional is very similar to that of the SH (Eq. 2.36), which is why the PFC model can also be treated as a conserved version of the SH equation [34].

3.2 The conserved Swift-Hohenberg (cSH) equation

The important difference to the SH equation is that not the free-energy, but the grand canonical potential

$$\Omega = \mathcal{F} - \int_0^L \mu u \, dx. \tag{3.13}$$

needs to be minimized due to mass conservation. This implies that the functional derivative of the free-energy is not supposed to be zero, but supposed to equal the chemical potential.

$$\frac{\delta \Omega[u]}{\delta u} = 0 \quad \Rightarrow \quad \mu = \frac{\delta \mathcal{F}[u]}{\delta u} \tag{3.14}$$

We therefore have to include the chemical potential in the stationary states, which now need to satisfy

$$\mu = ru + (q_c^2 + \partial_x^2)^2 u + u^3. \tag{3.15}$$

As for the SH equation r is the control parameter and q_c the critical wavenumber. Mass conservation, in the context of the order parameter field u, corresponds to the average of u over the whole domain.

$$\overline{u} = \int_0^L u \, dx \tag{3.16}$$

The dynamical order parameter equation can be obtained by setting

$$\partial_t u = \partial_x^2 \frac{\delta \mathcal{F}}{\delta u}. \tag{3.17}$$

The spatial derivatives ensure that mass conservation and the chemical potential are implicitly included in the dynamical equation. The conserved Swift-Hohenberg equation finally reads

$$\partial_t u = \partial_x^2 \left[ru + \left(\partial_x^2 + q_c^2\right)^2 u + u^3 \right], \tag{3.18}$$

and is indeed identical to the SH equation except for the second order derivative. $u(x,t) = \overline{u}$ is a homogeneous solution of the cSH and its dispersion relation is derived in the next section.

3.2.1 Linear stability analysis

As explained in section 2.2.2 we perform a linear stability analysis by adding an infinitesimal small perturbation $\tilde{u}(x,t) \sim \epsilon e^{iqx+\sigma t}$ to the homogeneous solution and linearising Eq. (3.18) in $\tilde{u}$..

$$\partial_t \tilde{u}(x,t) = \mathcal{L}\left[\,\overline{u}\,\right] \tilde{u}(x,t) + \mathcal{O}(\epsilon) \tag{3.19}$$

$$\Leftrightarrow \quad \sigma \tilde{u}(x,t) = -q^2 \left[r + \left(q_c^2 - q^2\right)^2 + 3\,\overline{u}^2 \right] \tilde{u}(x,t) \tag{3.20}$$

$$\Leftrightarrow \quad \sigma = -q^2 \left[r + \left(q_c^2 - q^2\right)^2 + 3\,\overline{u}^2 \right] \tag{3.21}$$

Like the original solution, $\tilde{u}(x)$ shall also satisfy periodic boundary conditions.

$$\tilde{u}(x+L) = \tilde{u}(x) \quad \Leftrightarrow \quad L = \frac{2\pi}{q} \tag{3.22}$$

The resulting dispersion relation

$$\mathcal{O}(\epsilon): \quad \sigma(q) = -q^2((q_c^2 - q^2)^2 + r + 3\overline{u}^2) \tag{3.23}$$

is very similar to that of the original SH equation but differs by the factor of q^2. That factor ensures that σ is always zero for $q = 0$ (see Fig. 3.1), a property well known from systems with conversation laws [24]. The flat solutions $\overline{u}$ become unstable to perturbations as r exceeds $r_c = -3\overline{u}^2$.

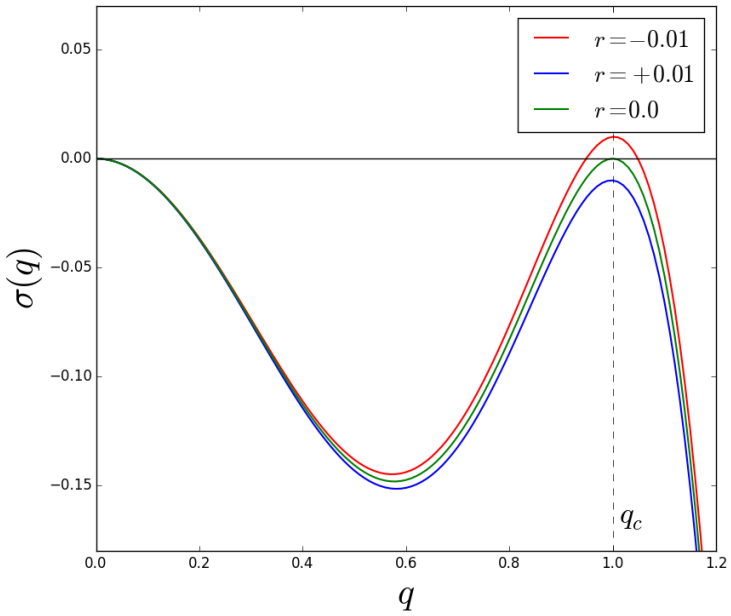

Figure 3.1: Dispersion relation of $\overline{u} = 0$ as a function of q, plotted for different r. The critical wavenumber $q_c = 1.0$ is marked by the dashed line.

3.2.2 Localised and periodic states

As for the SH we expect periodic and localised states to branch off when the flat solution $\overline{u}$ becomes unstable. Linear stability analysis predicted this to happen at $r_c = -3\overline{u}$. A weakly nonlinear approach can verify that this is indeed the case, but we will only refer to those calculations in [34, 24]. Instead we use the numerical continuation tool AUTO07 to find these periodic and localised stationary states.
Also we do no longer use r as the control parameter, but $\overline{u}$, so that the critical parameter becomes $\overline{u}_c = \pm\sqrt{-\frac{r}{3}}$. We restrict ourselves to the negative values

for $\overline{u}$ from here on, because positive $\overline{u}$ merely produce a mirrored image. The results of the numerical calculations are plotted in Fig. 3.2. One can see that the periodic solution branches off the flat solution $\overline{u}$ at $\overline{u}_c = \frac{1}{\sqrt{2}}$ as predicted from linear stability analysis. The localised solutions emerge in a secondary bifurcation from the periodic solution, because of the finite domain size (this could also be seen for the SH equation, see Fig. 2.5). As for the SH, the localised solutions undergo numerous saddle-node bifurcations before reaching the periodic state. The snaking does not occur in a bounded region this time, but is slanted which is typical for a system with a conserved quantity [34].

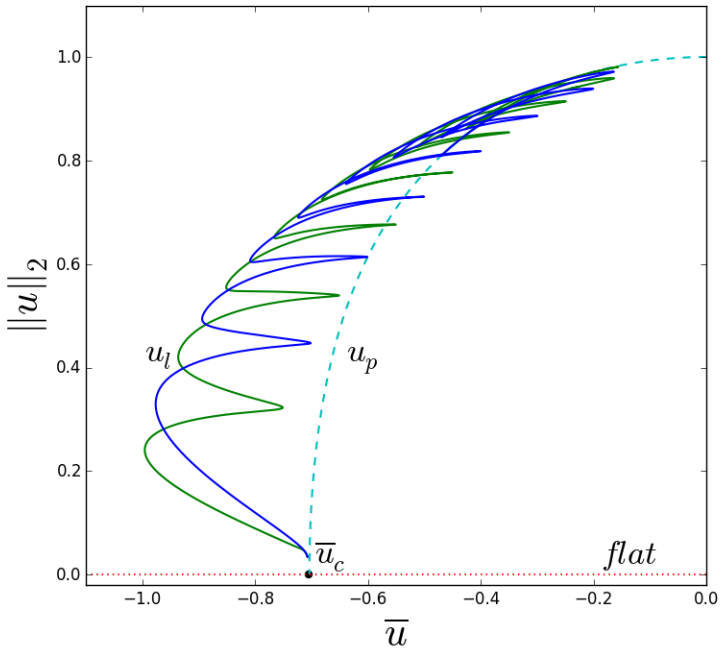

Figure 3.2: Flat, periodic and localised solutions of the conserved Swift-Hohenberg equation as a function of $\overline{u}$ for $r = -1.5$ and $q_c = 1.0$. The dotted red line corresponds to the flat solution $u(x) = \overline{u}$, the cyan dashed line to the periodic solution u_p with 15 bumps and the green and blue lines to localised solutions u_l with an odd and even number of bumps, respectively.

As a conclusion, the PFC model describes the transition from uniform state towards periodic or localised state very similar to the SH. Noticeably, the localised states undergo the snaking process as well.

4 Active phase field crystal (aPFC) model

While the PFC model is very useful in describing the transition from uniform states to resting crystalline states, it cannot describe travelling crystalline states. That is of great interest for many applications though [23], which is why the model needs to be expanded in order to describe active matter. Menzel and Löwen suggested a coupling with a polar ordering field [25, 26], which itself had been motivated by the Toner-Tu theory of self-propelled particles [35]. In its variational form this so-called active phase field crystal (aPFC) model is given by

$$\partial_t u = \partial_x^2 \frac{\delta \mathcal{F}}{\delta u} - v_0 \partial_x p, \tag{4.1}$$

$$\partial_t p = \partial_x^2 \frac{\delta \mathcal{F}}{\delta p} - D_r \frac{\delta \mathcal{F}}{\delta p} - v_0 \partial_x u. \tag{4.2}$$

v_0 is the strength of the self-propulsion and D_r the rotational diffusion constant. The average mean of u is still conserved in this model and the free-energy functional $\mathcal{F}$ needs to be expanded by a p-dependent term and now reads

$$\mathcal{F} = \int dx \left(\frac{u}{2} \left(r + (q_c^2 + \partial_x^2)^2 \right) u + \frac{u^4}{4} \right) + \int \frac{c_1}{2} p^2 \, dx. \tag{4.3}$$

Note that the coupling term itself is non-variational, meaning that Hopf bifurcations and temporally oscillating states are theoretically possible in this model as opposed to the PFC model. We should also mention that the functional for p falls short of the quartic term in comparison with the model proposed by [25, 26]. That term corresponds to spontaneous ordering and is here omitted for simplification. The order parameter equations of the aPFC model are given by

$$\partial_t u = \partial_x^2 \left(\left[r + (q_c^2 + \partial_x^2)^2 \right] u + (\overline{u} + u)^3 \right) - v_0 \partial_x p, \tag{4.4}$$

$$\partial_t p = -c_1 (D_r - \partial_x^2) p - v_0 \partial_x u. \tag{4.5}$$

Like in the PFC model, there are flat homogeneous states $(u, p) = (\overline{u}, 0)$. We will hence perform a linear stability analysis to determine their stability towards resting and travelling crystalline states. After that, the onset of motion from the resting to travelling crystalline states is explained in some detail. Throughout the thesis the parameters

$$r = -1.5, \quad D_r = 0.5, \quad c_1 = 0.1, \quad q_c = 1.0 \tag{4.6}$$

are fixed and only v_0 and $\overline{u}$ are varied.

4.1 Linear Stability Analysis

First we rewrite the order parameter equation by employing vector notation $\vec{u} = (u, p)$, so that

$$\partial_t \begin{pmatrix} u \\ p \end{pmatrix} = \begin{pmatrix} \partial_x^2 \left[r + (q_c^2 + \partial_x^2)^2 \right] & -v_0 \partial_x \\ -v_0 \partial_x & c_1(\partial_x^2 - D_r) \end{pmatrix} \begin{pmatrix} u \\ p \end{pmatrix} + \begin{pmatrix} \partial_x^2 (u + \overline{u})^3 \\ 0 \end{pmatrix}. \quad (4.7)$$

We then linearise Eq. (4.7) by introducing the perturbation $\vec{u}(x,t) = \epsilon e^{\lambda t + iqx} \vec{v}$ about the homogeneous state and end up with

$$\lambda \vec{v} = \underbrace{\begin{pmatrix} -q^2 \left[r + 3\overline{u}^2 + (q_c^2 - q^2)^2 \right] & -iqv_0 \\ -iqv_0 & -c_1(q^2 + D_r) \end{pmatrix}}_{:=\underline{L}} \vec{v}. \quad (4.8)$$

The matrix $\underline{L}$ has two eigenvalues which are

$$\lambda_\pm = \frac{1}{2} \left(\mathrm{Tr}(\underline{L}) \pm \sqrt{\mathrm{Tr}(\underline{L})^2 - 4 \det(\underline{L})} \right). \quad (4.9)$$

The flat homogeneous state is only linearly stable, if the real part of both eigenvalues is negative. As soon as the real part of one of the eigenvalues becomes positive, the perturbation evolves and the flat state is hence unstable. It is crucial though, whether the imaginary part of that eigenvalue is zero or not. In case it is indeed zero, the perturbation is not time-dependent and that is therefore called a stationary instability. If on the other hand, there is a non-vanishing imaginary part as the real part becomes positive, there is a time dependence in the perturbation. That is called an oscillatory instability. In the context of the PFC model, a stationary instability corresponds to the transition from a uniform state towards a resting crystalline state while an oscillatory instability corresponds to the transition from a uniform state towards a travelling crystalline state.
By looking at Eq. (4.9), we can see that an oscillatory instability occurs when the trace is zero and the determinant is positive. A stationary instability occurs when the determinant is zero and the trace is negative. In the following we will calculate when these instabilities arise in dependence of $\overline{u}$ and v_0, so that we end up with a phase diagram of flat states, resting crystals and travelling crystals.

4.1.1 Oscillatory instability

As mentioned before, the oscillatory instability arises when the trace of $\underline{L}$, which explicitly reads

$$\mathrm{Tr}(\underline{L}) = -q^2 \left[r + 3\overline{u}^2 + (q_c^2 - q^2)^2 \right] - c_1(q^2 + D_r), \quad (4.10)$$

is zero. Our goal is to find the parameter values $\overline{u}$ and v_0 for which this is the case. We start the calculations by setting Eq. (4.10) to zero and arrange the equation in q.

$$q^6 - 2q_c^4 q^2 + (r + 3\overline{u}^2 + q_c^4 + c_1)q^2 + c_1 D_r = 0 \quad (4.11)$$

By rebranding the parameters to

$$a = -2q_c^4, \tag{4.12}$$
$$b = r + 3\overline{u}^2 + q_c^4 + c_1, \tag{4.13}$$
$$c = c_1 D_r \tag{4.14}$$

and substituting q^2 with y this simplifies to the cubic equation

$$y^3 + ay^2 + by + c = 0. \tag{4.15}$$

This can be solved by using Cardano's formula [5]. Since q represents a positive real valued wavenumber, we are only interested in positive real solutions for y. Additionally we want to find the parameter values $\overline{u}$ and v_0 for which this happens the first time. According to Cardano's formula, the first real valued root appears at

$$y = 2\sqrt[3]{\frac{9ab - 27c - 2a^3}{54}} - \frac{a}{3} \tag{4.16}$$

under the condition that

$$\left(\frac{3b - a^2}{9}\right)^3 + \left(\frac{9ab - 27c - 2a^3}{54}\right)^2 = 0. \tag{4.17}$$

With the parameter choices of Eq. (4.6) we have the two Eq. (4.16),(4.17) and the two unknowns q and $\overline{u}$. Note that v_0 does not appear in the trace (Eq. 4.10). After solving the equations we find that

$$\overline{u} = -0.671, \qquad q = 1.012. \tag{4.18}$$

Finally, this gives us the border between the flat state and travelling crystals.

4.1.2 Stationary instabilty

Now we apply the same procedure to the stationary instability. The determinant in its explicit form is given by

$$\det(\underline{L}) = q^2 \left[r + 3\overline{u}^2 + (q_c^2 - q^2)^2\right] c_1(q^2 + D_r), \tag{4.19}$$

and needs to be set to zero in order to find an equation for q.

$$q^6 + (D_r - 2q_c^4)q^2 + (r + 3\overline{u}^2 + q_c^4 - 2q_c^2 D_r)q^2 + \frac{v_0^2}{c_1} + D_r(r + 3\overline{u}^2 + q_c^4) = 0 \tag{4.20}$$

As before we substitute q^2 with y to end up with the cubic equation for y (Eq. 4.15), but the parameters a, b and c are a little different in this case.

$$a = D_r - 2q_c^4 \tag{4.21}$$
$$b = r + 3\overline{u}^2 + q_c^4 - 2q_c^2 D_r \tag{4.22}$$
$$c = \frac{v_0^2}{c_1} + D_r(r + 3\overline{u}^2 + q_c^4) \tag{4.23}$$

The most important difference is that v_0 appears in the parameters, meaning that we have the three unknowns $\overline{u}$, v_0 and q only the two equations (4.16) and (4.17). We therefore approximate q with 1, which is the exact solution for the PFC model (see section 3.2.1), and find that

$$\overline{u} \approx -\sqrt{\frac{1}{2} - \frac{20}{9}v_0^2}. \tag{4.24}$$

The wavenumber approximation had also been used in [9], where the same conceptual results for the linear stability analysis had been found. Eq. (4.24) denotes the border between the flat state and resting crystals. Note that for $v_0 = 0$ this is in perfect agreement with the dispersion relation of the PFC model, as expected.

4.1.3 Phase diagram

The derived borders are plotted in Fig. 4.1 and are in very good agreement with numerical results obtained with AUTO07. The transition from resting to travelling states is described in detail in the next section.

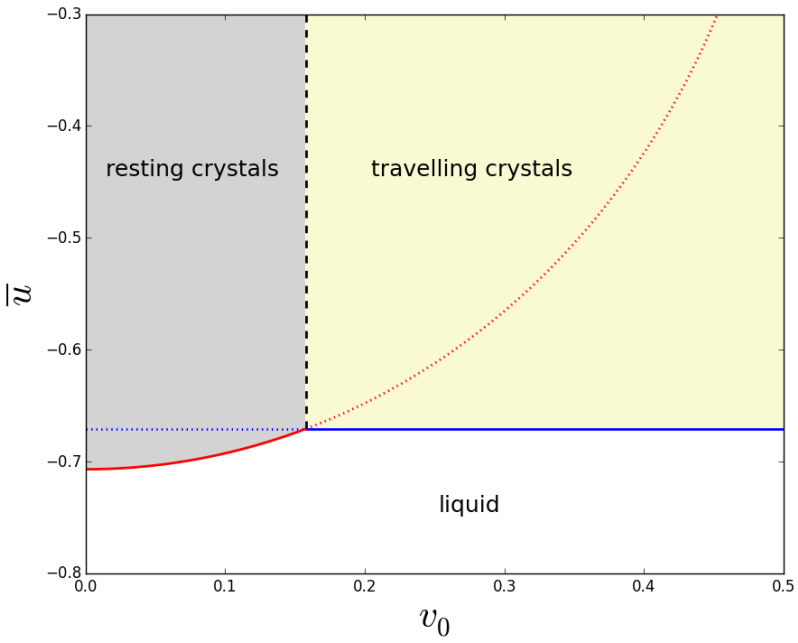

Figure 4.1: Phase diagram of the aPFC model in $\overline{u}$ and v_0. The red line (Eq. 4.24) divides the liquid phase (white) from the resting crystal phase (grey), whereas the blue line (Eq. 4.18) divides the liquid phase from the travelling crystal phase (yellow). The dashed black line at $v_0 \approx 0.158$ indicates where the first imaginary eigenvalues appear and therefore mark the border between resting and travelling crystals.

4.2 Drift Bifurcation - Onset of Motion

In this section we paraphrase the derivation of the drift bifurcation as proposed by Ophaus et al. [28] and show that the resting states undergo a drift instability. We start by reframing the order parameter equation (Eq. 4.5) in terms of a co-moving frame with velocity v and expand the order parameter field around a stationary state $(u_0(\xi), p_0(\xi))$ of the co-moving frame ($\xi = x - vt$).

$$u = u_0(\xi) + v u_1(\xi) + \mathcal{O}(v^2) \tag{4.25}$$

$$p = p_0(\xi) + v p_1(\xi) + \mathcal{O}(v^2) \tag{4.26}$$

Introduced into the order parameter equation, the first order of v reads

$$\partial_\xi \begin{pmatrix} u_0 \\ p_0 \end{pmatrix} = \underbrace{\begin{pmatrix} \partial_\xi^2 \left(\left[r + (1+\partial_\xi^2)^2 \right] + 3(\overline{u}+u_0)^2 \right) & -v_0 \partial_\xi \\ -v_0 \partial_\xi & c_1(\partial_\xi^2 - D_r) \end{pmatrix}}_{:=\underline{L}(u_0)} \begin{pmatrix} u_1 \\ p_1 \end{pmatrix}. \tag{4.27}$$

The aPFC order parameter equations are translational invariant, which implies that the spatial derivative of a stationary state is a neutral eigenmode of $\underline{L}$ [22].

$$\underline{L}(u_0) \cdot \partial_\xi \begin{pmatrix} u_0 \\ p_0 \end{pmatrix} = 0 \quad \Rightarrow \quad \partial_\xi \begin{pmatrix} u_0 \\ p_0 \end{pmatrix} = \mathcal{G} \tag{4.28}$$

The neutral eigenmode is often called the Goldstone mode $\mathcal{G}$ in this context. Eq. (4.27) implies that $\underline{L}$ operating on (u_1, p_1) yields the Goldstone mode, which makes (u_1, p_1) a generalized eigenmode, also called the Propagator mode $\mathcal{P}$. We therefore end up with the equation

$$L\mathcal{P} = \mathcal{G}, \tag{4.29}$$

which only has a solution if the Fredholm Alternative is satisfied [17]. The solvability condition reads

$$\langle \mathcal{G}^\dagger | \mathcal{G} \rangle = 0, \tag{4.30}$$

where $\mathcal{G}^\dagger$ is defined by

$$L^\dagger \mathcal{G}^\dagger = 0. \tag{4.31}$$

It has been derived by Ophaus et al. [28] that Eq. (4.30) is fulfilled exactly when

$$\|u_0\|_{L^2} = \|p_0\|_{L^2}, \tag{4.32}$$

where $\| \cdot \|_{L^2}$ is the L^2-Norm. Eq. (4.32) gives us an analytical criterium with which we are able to predict the onset of motion for resting states. This result proved to be extremely helpful in finding numerous branches of travelling localised states, which are the main topic of the next section.

5 Localised states in the aPFC model

In this section we give an extensive overview over the localised states (both resting and travelling) of the aPFC model and highlight their bifurcation behaviour depending on v_0 and $\overline{u}$. We focus on the continuation in v_0, since the linear stability analysis showed that the onset of motion is largely independent from $\overline{u}$ (see Fig. 4.1).
The starting point of our investigation is the bifurcation diagram of the PFC model (Fig. 3.2), since the two models are identical for $v_0 = 0$ when the aPFC model is decoupled. Therefore, we only need to continue the given solutions with respect to v_0, which is done by using the numerical continuation tool AUTO07. The domain size of $L = 100$ is held constant throughout this thesis. Seven exemplary values of $\overline{u}$ have been chosen for continuation (see Fig. 5.1) to demonstrate how numerous branches of travelling localised states come into existence.

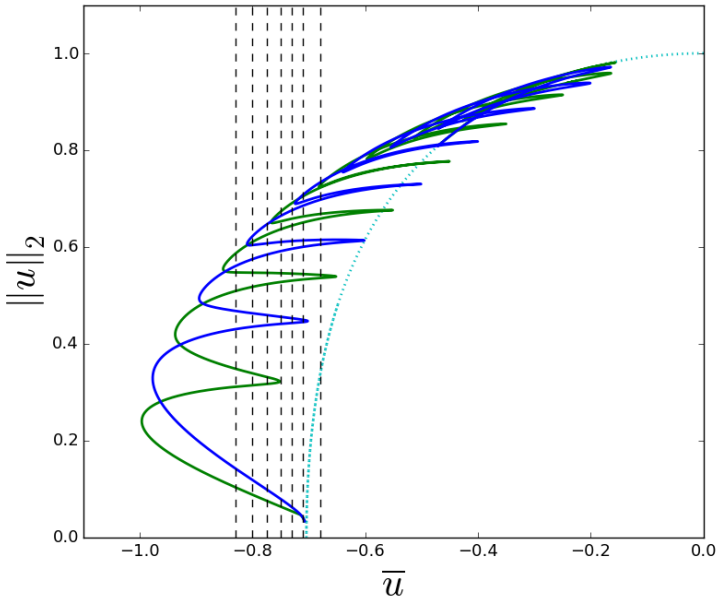

Figure 5.1: Bifurcation diagram of the aPFC model for $v_0 = 0$. It shows a periodic 15-bump solution (dotted cyan), a branch of localised solutions with an odd number of bumps (green) and one with an even number of bumps (blue). The straight dashed lines are at -0.83, -0.80, -0.775, -0.75 ,-0.73, -0.71 and -0.68, and represent the values of $\overline{u}$ from which the continuation in v_0 will take place.

After a thorough investigation in the bifurcation diagrams in v_0 in section 5.1,

there will be short presentation of the bifurcation diagrams as a function of $\overline{u}$ in sec. 5.2. Finally fold continuation in v_0 and $\overline{u}$ is performed in sec. 5.3.

5.1 Continuation in v_0

In the following we will present the bifurcation diagram of v_0 for the seven marked values of $\overline{u}$ in Fig. 5.1. Interesting bifurcation behaviour will be explained in detail.

5.1.1 $\overline{u} = -0.83$: Initial appearance of travelling single-bumps

As expected from the PFC bifurcation diagram (Fig.5.1), we find five branches of resting localised states for $\overline{u} = -0.83$, from single-bumps to quintuple-bumps (Fig. 5.2). Branches with fewer bumps exist on a wider domain of v_0 and only the single-bump branch stretches far enough to satisfy the solvability condition $\|u\|_2 = \|p\|_2$. This is visually demonstrated by Fig. 5.3, where the L2-Norm differences of u and p are plotted for all localised states. Apparently, only the resting localised state fulfils the condition at two spots. Therefore, we can observe the onset of two branches of travelling localised single-bumps, which grow directly out of the fold of the resting single-bump branch (Fig. 5.2). Since the resting state loses its stability to two travelling states with opposite velocity, it is a pitchfork bifurcation. The density and polarization of an exemplary single-bump are shown in Fig. 5.4. While resting states are symmetric, the travelling state is a little asymmetric. In that sense, the drift instability corresponds to a symmetry breaking.

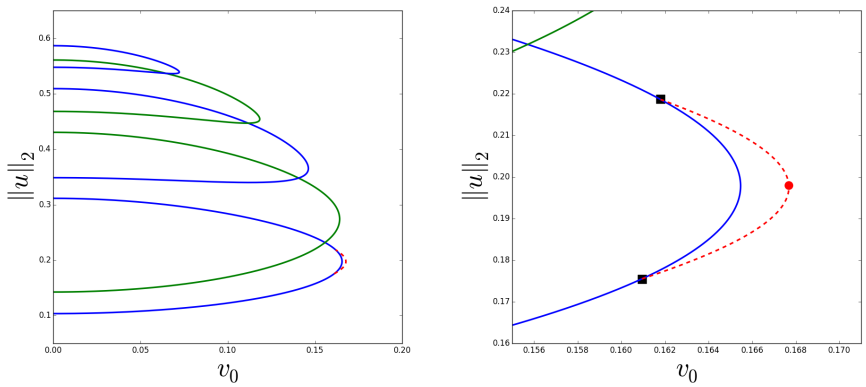

Figure 5.2: Bifurcation diagram as a function of v_0 for $\overline{u} = -0.83$. Resting localised states with an odd number of bumps are depicted blue, those with an even number of bumps green. The right hand side shows a close-up of the branches of travelling localised single-bumps, which are shown in red (dashed line). The red circle marks the single-bump plotted in Fig. 5.4 and the black squares mark the pitchfork bifurcations.

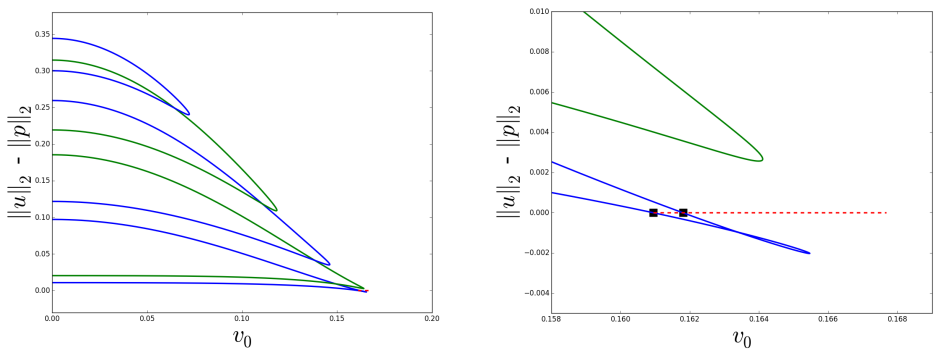

Figure 5.3: Difference in the L2-Norms of $u(x)$ and $p(x)$ as a function of v_0 for all localised states at $\overline{u} = -0.83$. Note that among the resting localised states, only the resting single-bump branch becomes negative, which is shown in more detail in the close-up on the right hand side. The travelling localised state (red dashed line) is always zero, as required from the solvability condition. The black square markers indicate the pitchfork bifurcations and are the same as in Fig. 5.2.

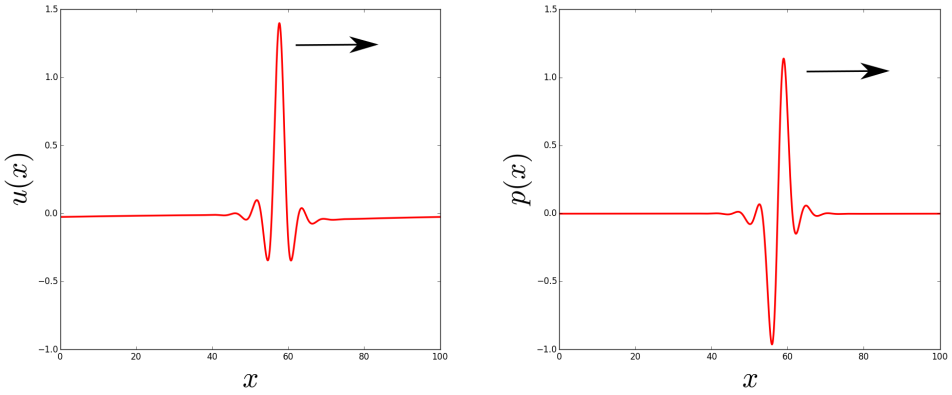

Figure 5.4: Density and polarisation profile, $u(x)$ and $p(x)$ respectively, for $\overline{u} = -0.83$ and $v_0 = 0.1677$ of a travelling single-bump with a velocity of $v = 0.0446$. The direction of motion is indicated by the black arrows.

5.1.2 $\overline{u} = -0.80$: Appearance of travelling double-bumps

In comparison to $\overline{u} = -0.83$, an additional resting sextuple-bump branch appears on top of the other branches and additionally a branch of travelling double-bumps comes into existence, since the resting double-bump branch stretches further out (see Fig. 5.5). This time the structure of the localised double-bumps looks quite different in comparison with the single-bump structure. Instead of one, there are now three saddle-node bifurcations and the whole structure is inside, not outside its resting equivalent. Also the travelling single-bump branch has grown considerably. The density and polarization profiles of an exemplary double-bump are shown in Fig. 5.6. Like the travelling single-bump, the travelling double-bump is a little asymmetric.

The different onset of the travelling double-bumps is further investigated by taking smaller steps in $\overline{u}$. Fig. 5.7 shows the process in four steps. The travelling double-bump branch comes into existence via two drift-pitchfork bifurcations, as can be seen in the figure in the top left corner at $\overline{u} = -0.824$. As $\overline{u}$ increases, saddle-node bifurcations gradually appear until the branch takes the form that had been observed in Fig. 5.5.

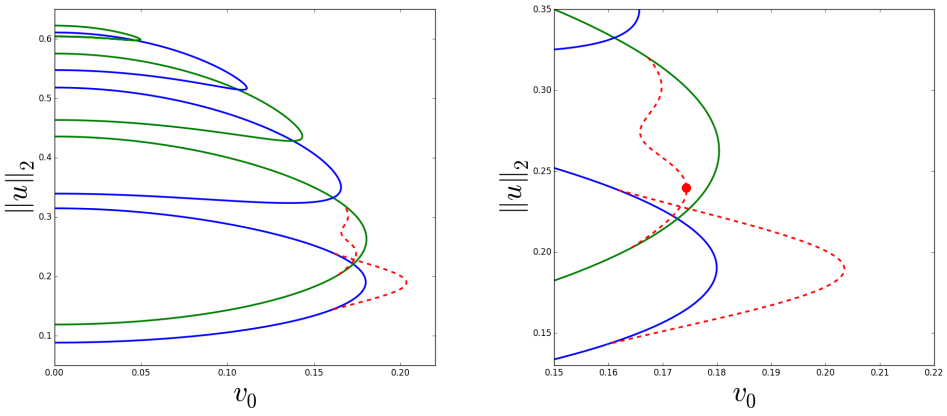

Figure 5.5: Bifurcation diagram as a function of v_0 for $\overline{u} = -0.80$. Resting localised states with an odd number of bumps are depicted blue, those with an even number of bumps green. The right hand side shows a close-up of the branches of travelling localised single- and double-bumps, which are depicted in red (dashed lines). The red circle marks the double-bump plotted in Fig. 5.6.

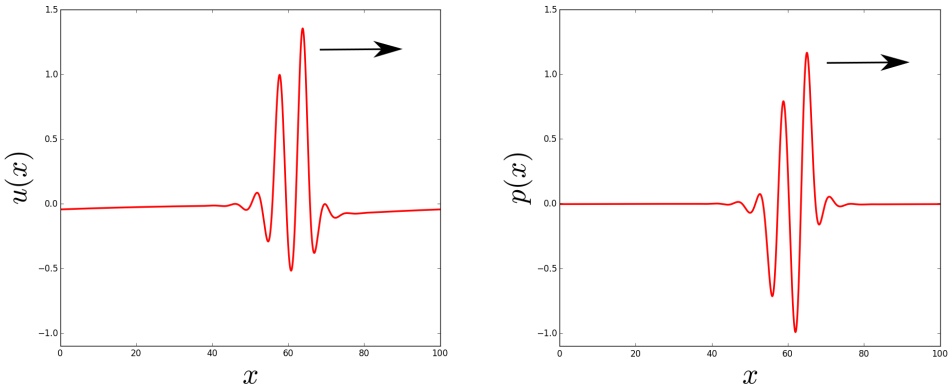

Figure 5.6: Density and polarization profile, $u(x)$ and $p(x)$ respectively, for $\overline{u} = -0.80$ and $v_0 = 0.1744$ of a travelling double-bump with a velocity of $v = 0.0551$. The direction of motion is indicated by the black arrows.

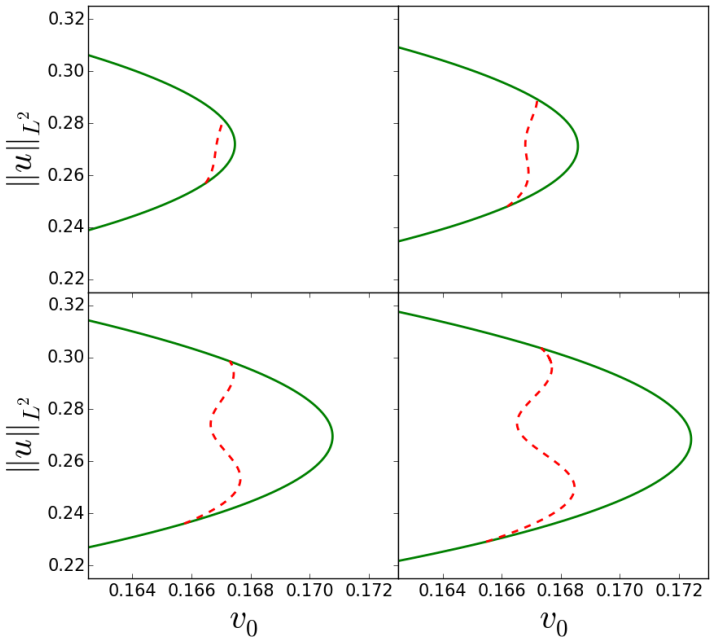

Figure 5.7: Bifurcation diagram of the travelling double-bumps for different values of $\overline{u}$ ($-0.824, -0.822, -0.818$ and -0.815 from left to right). The travelling double-bump branch is depicted in red (dashed lines), the resting double-bump branch in green.

5.1.3 $\overline{u} = -0.775$: Appearance of travelling triple-bumps

As before, all branches stretch over a broader domain of v_0 as $\overline{u}$ rises. This time, the resting triple-bump branch stretches far enough that the solvability condition is satisfied and a branch of travelling triple-bumps appears. The way they come into existence is identical to that of the branch of travelling double-bumps, which was shown in Fig. 5.7. An exemplary triple-bump is plotted in Fig. 5.9. A noticeable difference to the branch of double-bumps is, that it exists on a much smaller domain of v_0. It should also be noted that both the single-bump branch and the lower of the double-bump branches keep growing as $\overline{u}$ is increasing.

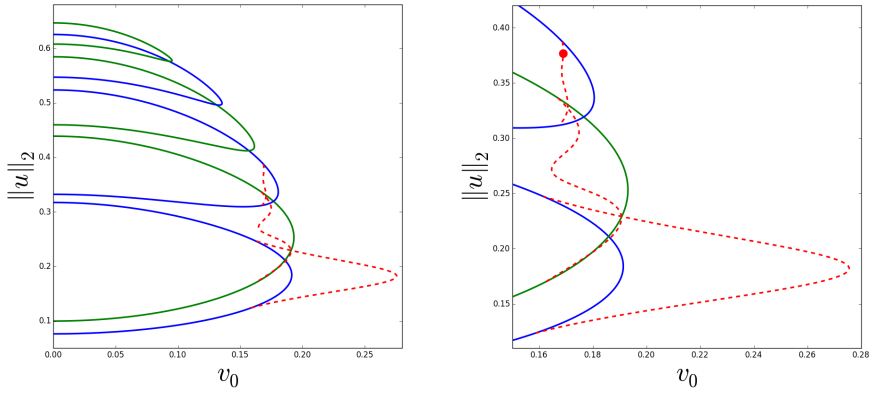

Figure 5.8: Bifurcation diagram as a function of v_0 for $\overline{u} = -0.775$. Resting localized states with an odd number of bumps are depicted blue, those with an even number of bumps green. The right hand side shows a close-up of the branches of travelling localised single-, double- and triple-bumps, which are depicted in red (dashed lines). The red circle marks the triple-bump plotted in Fig. 5.9.

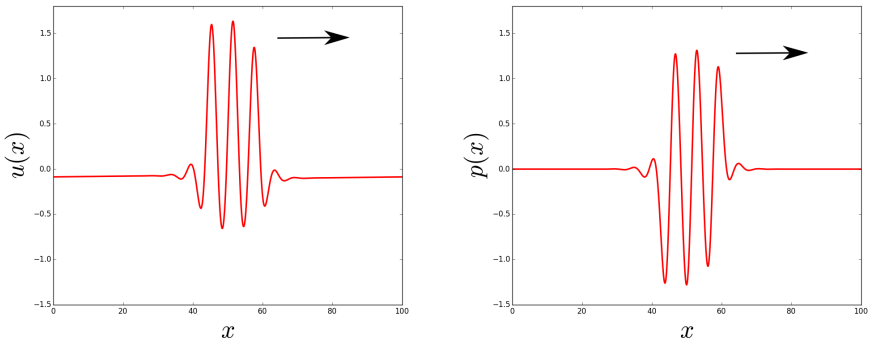

Figure 5.9: Density and polarization profile, $u(x)$ and $p(x)$ respectively, for $\overline{u} = -0.775$ and $v_0 = 0.1691$ of a travelling triple-bump with a velocity of $v = 0.0120$. The direction of motion is indicated by the black arrows.

5.1.4 $\overline{u} = -0.75$: Appearance of travelling quadruple-bumps

At $\overline{u} = -0.75$ a resting septuple-bump branch appears and there is also a new branch of travelling quadruple-bumps branching off its resting equivalent. An exemplary quadruple-bump is plotted in Fig. 5.10. Its branch exists on an even smaller domain of v_0 (see Fig. 5.11), but its onset is otherwise identical to that of the double- and triple-bumps. Also as a novelty, the resting single- and triple-bump branches have merged by forming two separate saddle-node bifurcations. In comparison to $\overline{u} = -0.775$ (Fig. 5.8), the lower of the double-bump branches has continued to grow, while the single-bump branch has grown massively. All the other travelling localised states are confined in a region between $v_0 \approx 0.16$ and $v_0 \approx 0.19$.

We also compare the velocities of the various travelling localised states in Fig. 5.12. In general, localised states that stretch over a broader domain of v_0, also have a greater variety in velocities. At onset of motion, coupling parameter v_0 and drift velocity v are not proportional for all travelling localised state, but for larger v_0 this changes. For the branch of travelling localised single-bumps, v_0 and v are clearly proportional as v_0 gets larger than 0.4.

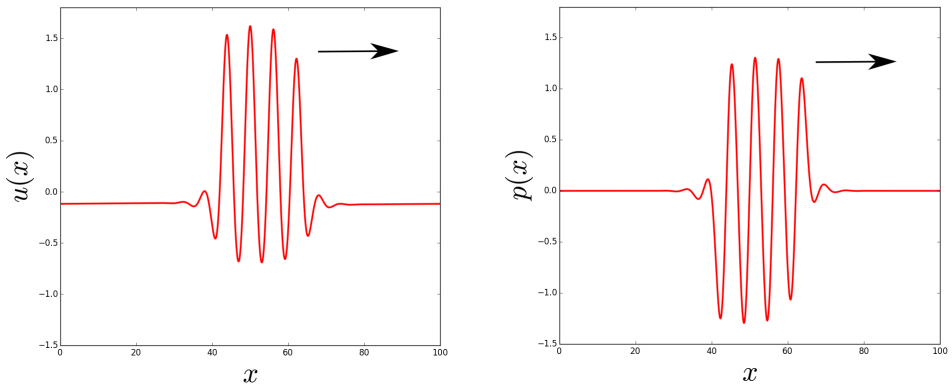

Figure 5.10: Density and polarization profile, $u(x)$ and $p(x)$ respectively, for $\overline{u} = -0.75$ and $v_0 = 0.1688$ of a travelling quadruple-bump with a velocity of $v = 0.0054$. The direction of motion is indicated by the black arrows.

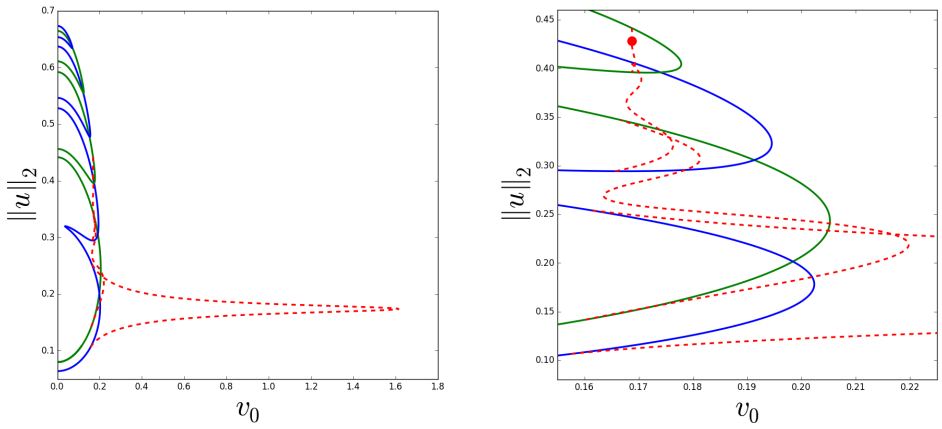

Figure 5.11: Bifurcation diagram as a function of v_0 for $\overline{u} = -0.75$. Resting localised states with an odd number of bumps are depicted blue, those with an even number of bumps green. The right hand side shows a close-up of the branches of travelling localised single-, double-, triple- and quadruple-bumps, which are depicted in red (dashed lines). The red circle marks the quadruple-bump plotted in Fig. 5.10.

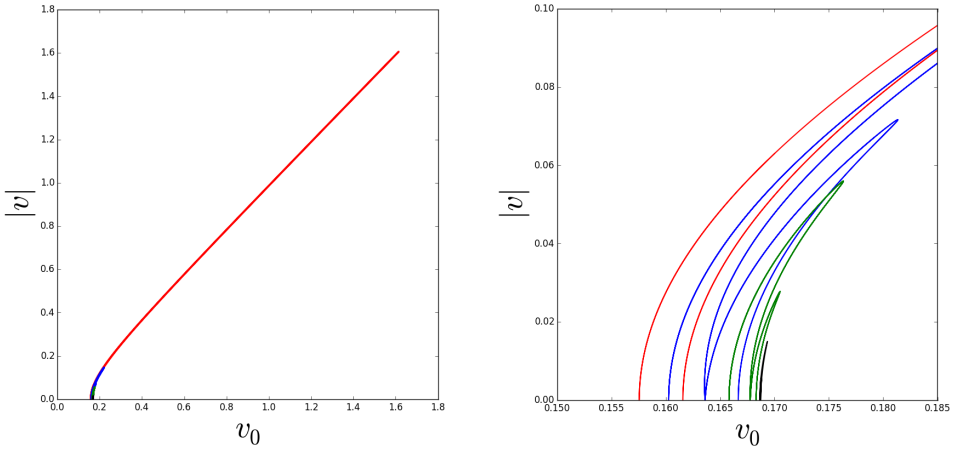

Figure 5.12: Absolute value of the drift velocity v for the travelling localised states as a function of v_0 at $\overline{u} = -0.75$. The right-hand side shows a close-up for small velocities. The travelling single-bump is depicted in red, the travelling double-bump in blue, the travelling triple-bump in green and the travelling quadruple-bump in black.

5.1.5 $\overline{u} = -0.73$: Divergence of single-bump branch, pinch-off bifurcation and appearance of travelling quintuple-bumps

For $\overline{u} = -0.73$ a new branch of travelling quintuple-bumps appears, while no new resting localised states come into existence. An exemplary quintuple-bump is plotted in Fig. 5.13. There are also two notable novelties when looking at the bifurcation diagram (Fig. 5.14). First the single-bump branch has completely diverged and seems to exist for infinitely large v_0. Also the lower and upper part of the single-bump branch are separated by a considerable distance. The second interesting new property is the loop that the single- and double-bump branches have formed, as can be seen at the right hand side of Fig. 5.14. The travelling states are at least partly disconnected with the resting states, which is why we refer to this process as a pinch-off bifurcation.

We now give a more detailed investigation of the pinch-off bifurcation by taking into account in-between values of $\overline{u}$. At $\overline{u} = -0.738$ the single- and double-bump branch are very close, almost parallel to each other (see Fig. 5.15). For increasing $\overline{u}$ the two branches get even closer at $v_0 \approx 0.17$, while there is very little change everywhere else. At $\overline{u} = -0.734$, the two branches have partly annihilated each other by forming two separate saddle-node bifurcation. For rising $\overline{u}$ the distance between the two saddle-node bifurcation points increases and the pinch-off bifurcation is complete.

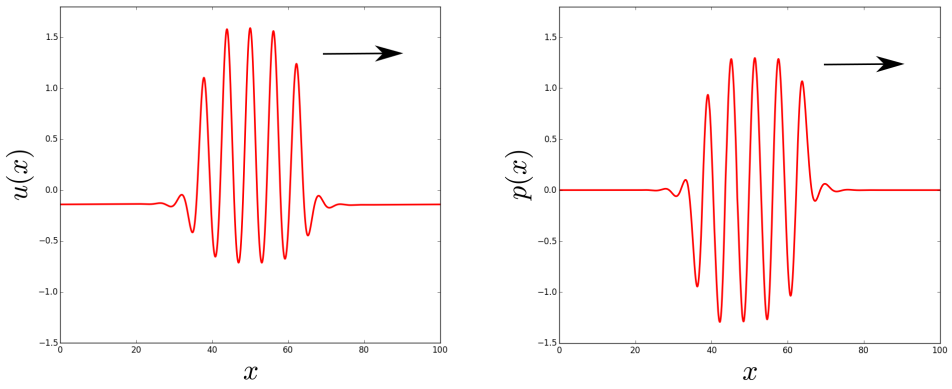

Figure 5.13: Density and polarization profile, $u(x)$ and $p(x)$ respectively, for $\overline{u} = -0.73$ and $v_0 = 0.1684$ of a travelling quintuple-bump with a velocity of $v = 0.0034$. The direction of motion is indicated by the black arrows.

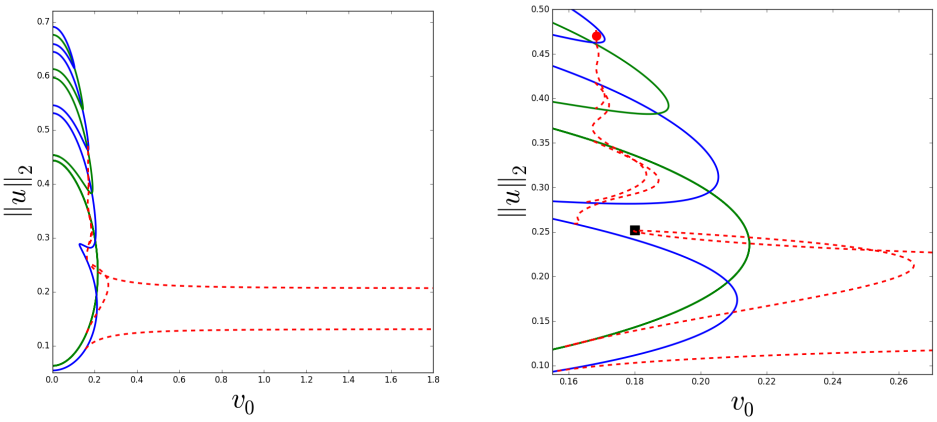

Figure 5.14: Bifurcation diagram as a function of v_0 for $\overline{u} = -0.73$. Resting localised states with an odd number of bumps are depicted blue, those with an even number of bumps green. The right hand side shows a close-up of the branches of travelling localised single-, double-, triple-, quadruple- and quintuple-bumps, which are depicted in red (dashed lines). The red circle marks the quintuple-bump plotted in Fig. 5.13 and the black square marks the pinch-off bifurcation.

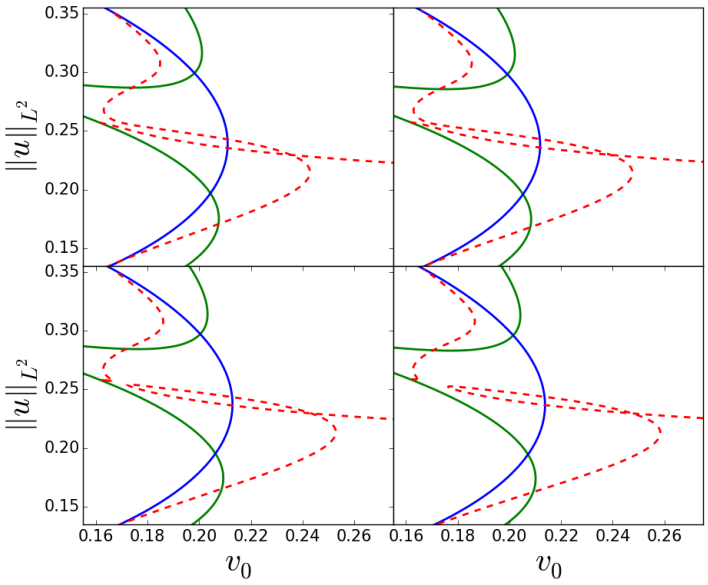

Figure 5.15: Pinch-off bifurcation diagram of the travelling single- and double-bumps for different values of $\overline{u}$ ($-0.738, -0.736, -0.734$ and -0.732 from top left to bottom right). The travelling localised states are shown in red (dashed lines), the odd resting localised states in blue and the even resting localised states in green.

5.1.6 $\overline{u} = -0.71$: Further pinch-off bifurcations and disappearance of travelling states

An additional resting octuple-bump branch has appeared and the structure of the travelling state branches looks noticeably different for $\overline{u} = -0.71$ (see Fig. 5.16). Apparently, further pinch-off bifurcations have occurred.
In order to explain this, we take smaller steps in $\overline{u}$ (see Fig. 5.17). In the beginning, at $\overline{u} = -0.73$, the branches have the familiar structure described before. As $\overline{u}$ increases numerous saddle-node bifurcations create an isolated region of travelling triple-bumps for $\overline{u} = -0.724$. We name this process again pinch-off bifurcation. The isolated structure exists only in a small parameter regime and has already completely vanished for $\overline{u} = -0.721$.
Also, from $\overline{u} = -0.73$ to $\overline{u} = -0.71$ the branch of travelling triple-bumps has disappeared. The exact procedure is shown in Fig. 5.18. Due to the pinch-off bifurcations the branch of travelling states connects the resting single-bumps with the resting triple-bumps at $\overline{u} = -0.728$. For increasing $\overline{u}$ the resting fold moves towards higher v_0 and the travelling branch hence disappears in it.

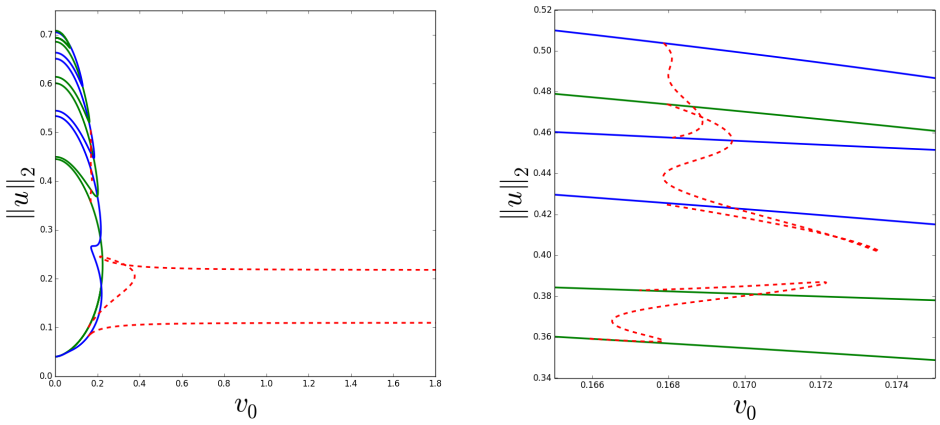

Figure 5.16: Bifurcation diagram as a function of v_0 for $\overline{u} = -0.71$. Resting localised states with an odd number of bumps are depicted blue, those with an even number of bumps green. The right hand side shows a close-up of the branches of travelling localised triple-,quadruple- and quintuple-bumps, which are depicted in red (dashed lines).

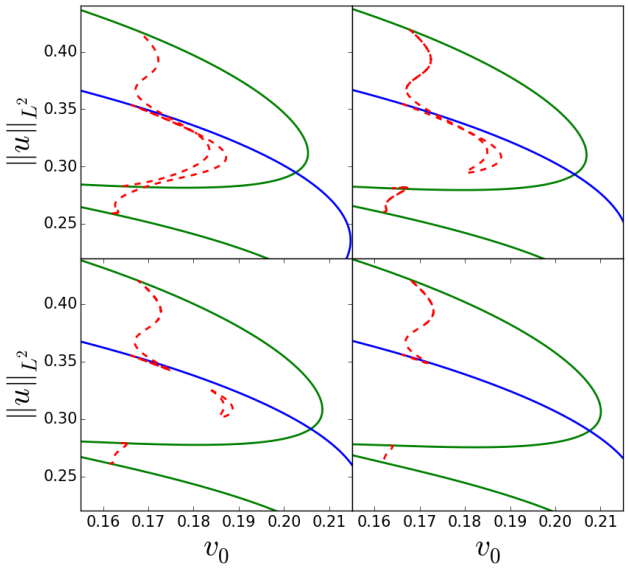

Figure 5.17: Pinch-off bifurcation diagram of the travelling double- and triple-bumps for different values of $\overline{u}$ ($-0.730, -0.727, -0.724$ and -0.721 from top left to bottom right). The travelling localised states are shown in red (dashed lines), the odd resting localised states in blue and the even resting localised states in green.

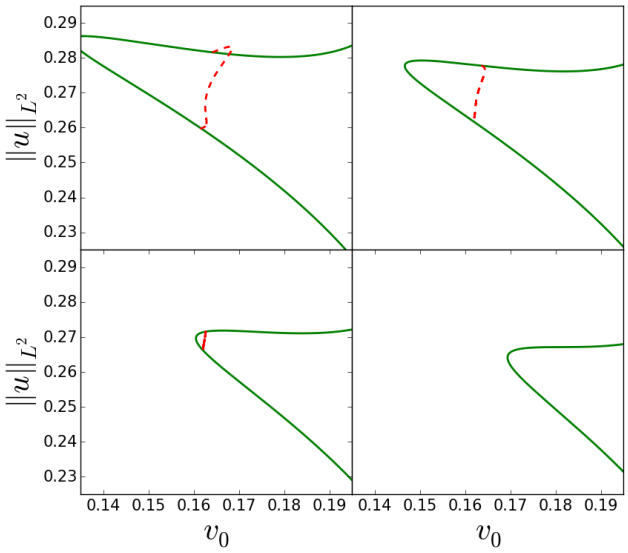

Figure 5.18: Bifurcation diagram depicting the disappearance of the travelling double-bumps for different values of $\overline{u}$ ($-0.728, -0.722, -0.715$ and -0.710 from top left to bottom right). The travelling localised states are shown in red (dashed lines) and the even resting localised states in green.

5.1.7 $\overline{u} = -0.68$: Appearance of periodic states and further pinch-off bifurcations

The lower double-bump branch that has grown continuously throughout our observation has now completely diverged, as had the single-bump branch before. Apart from that, a new branch of travelling sextuple-bumps appeared (see Fig. 5.19) and for the first time resting periodic states come into existence, which are depicted by a cyan line in Fig. 5.20. The behaviour of the travelling states repeats itself compared to the mechanism we have outlined earlier. Travelling states with a rising number of bumps come into existence, pinch-off and then disappear into the resting fold.

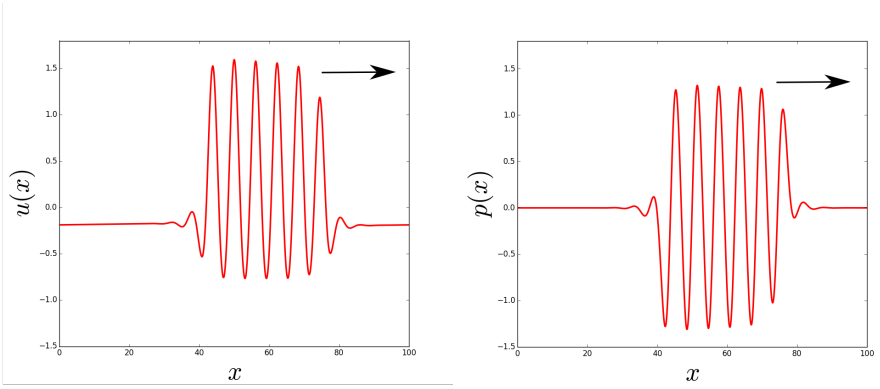

Figure 5.19: Density and polarization profile, $u(x)$ and $p(x)$ respectively, for $\overline{u} = -0.68$ and $v_0 = 0.1671$ of a travelling sextuple-bump with a velocity of $v = 0.0062$. The direction of motion is indicated by the black arrows.

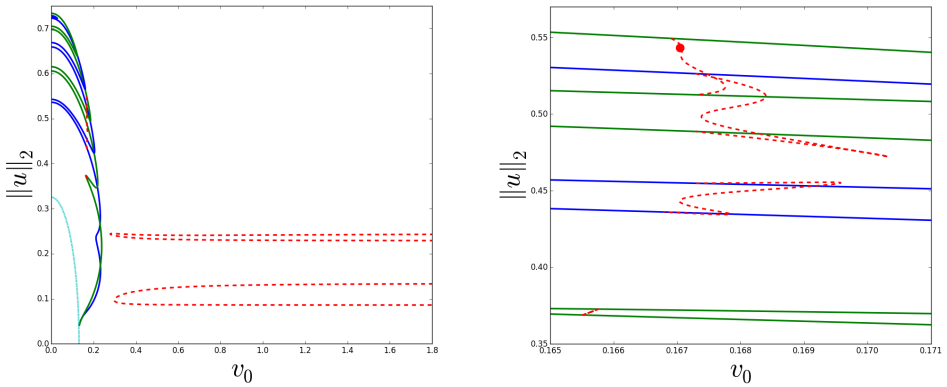

Figure 5.20: Bifurcation diagram as a function of v_0 for $\overline{u} = -0.68$. Resting localised states with an odd number of bumps are depicted blue, those with an even number of bumps green and the resting periodic 16-tuple bump cyan (dotted line). The right hand side shows a close-up of the branches of travelling localised triple-, quadruple-, quintuple- and sextuple-bumps which are depicted in red (dashed lines).

There is no qualitative new behaviour, which is why we end our analysis of the travelling localised states at $\overline{u} = -0.68$. It is also increasingly hard to obtain numerical results for the travelling multi-bump states, because their region of existence keeps shrinking. The influence of the periodic states is better explained when looking at the bifurcation diagram as a function of $\overline{u}$, which will be the topic of the next section.

5.2 Continuation in $\overline{u}$

In the following, we provide a short overview of the bifurcation diagram as a function of $\overline{u}$, but restrict ourself to only a few diagrams since most effects are already explained in the previous section.

5.2.1 $v_0 = 0.17$: Appearance of travelling localised states

From continuation in v_0, we expect that many of the travelling localised states exist for $v_0 = 0.17$, which is small but yet beyond the onset of motion. Indeed we can observe four loops (see Fig. 5.21, which correspond to loops of single- and double-bumps, double- and triple-bumps, triple- and quadruple-bumps and quadruple- and quintuple-bumps respectively. The loops for localised states with a higher number of bumps are noticeable smaller, hence exist on a much smaller region, which is in agreement with the results of the previous section. Travelling sextuple-bumps or bumps with an even higher tuple of bumps exist on such a small regime, that they have already disappeared for $v_0 = 0.17$. It also seems like the loops of travelling localised states grow out of the resting states, and then shrink as v_0 gets bigger. We should also note that the periodic state in Fig. 5.21 is not a 15-tuple bump as it had been for $v_0 = 0$, but a 16-tuple bump.

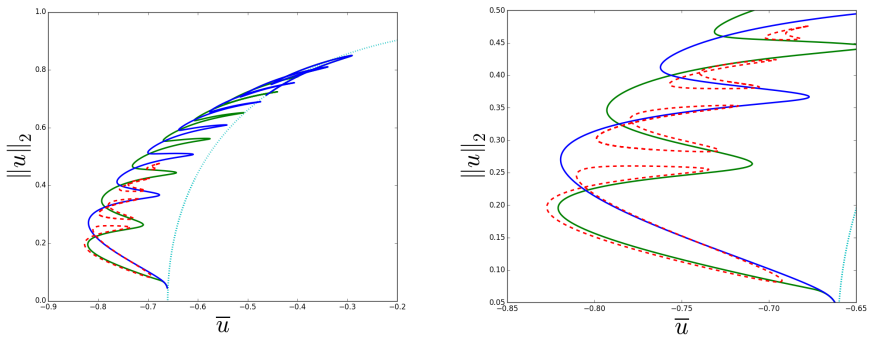

Figure 5.21: Bifurcation diagram as a function of $\overline{u}$ for $v_0 = 0.17$. Resting localised states with an odd number of bumps are depicted blue, those with an even number of bumps green. The periodic 16-bump solution is depicted in cyan and the travelling localized solutions in red, which are shown in a close-up on the right hand side.

5.2.2 $v_0 = 0.20$ & $v_0 = 0.25$: Disappearance and drift of travelling states

In comparison to $v_0 = 0.17$, only the first loop of single- and double-bumps has survived (see Fig. 5.22), while all other loops have vanished. This is again in agreement with what we had seen in the continuation of v_0. All travelling localised states exist only on a small bounded region of v_0, except for the single-bump branch and the lower double-bump branch. Those eventually diverged, which corresponds to a drift of the whole loop in the bifurcation diagram of $\overline{u}$. This is confirmed by the bifurcation diagram of $v_0 = 0.25$ (Fig. 5.23), where the drift continued and the loop is completely separated from the resting localised states. Again this is completely in agreement with the results of the continuation in v_0. Compare for example with $\overline{u} = -0.68$ (Fig. 5.20), where the travelling single- and double-bumps have also separated from the resting states. It is also well visible that the branches of the odd and even resting states move closer and closer together and seem to be just before annihilation at $v_0 = 0.25$. This is of course not unexpected considering the precious section, since the resting states there existed only until $v_0 \approx \pm 0.25$, almost independently from $\overline{u}$.

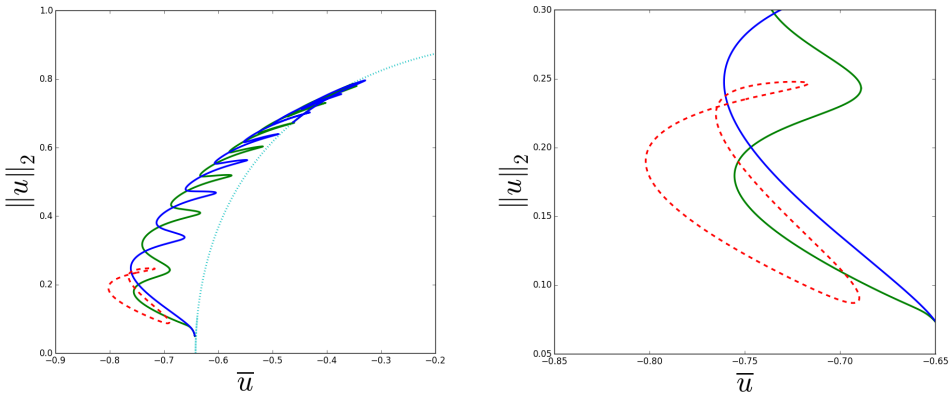

Figure 5.22: Bifurcation diagram as a function of $\overline{u}$ for $v_0 = 0.20$. Resting localized states with an odd number of bumps are depicted blue, those with an even number of bumps green. The periodic 16-tuple state is depicted in cyan and the travelling localized states in red, which are shown in a close-up on the right hand side.

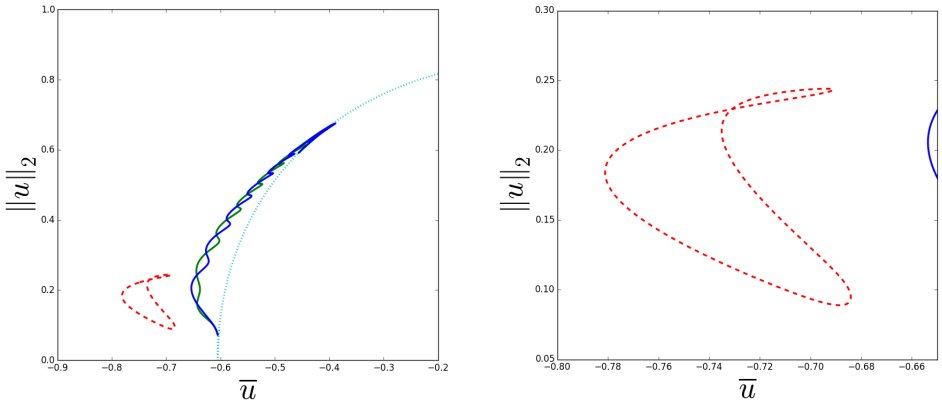

Figure 5.23: Bifurcation diagram as a function of $\overline{u}$ for $v_0 = 0.25$. Resting localized states with an odd number of bumps are depicted blue, those with an even number of bumps green. The periodic 16-tuple state is depicted in cyan and the travelling localized states in red, which are shown in a close-up on the right hand side.

5.2.3 $v_0 = 0.50$: Disappearance of resting localised states

For $v_0 = 0.5$ all resting localised states have vanished and there are only travelling localised states left. In fact only the loop of travelling localised single- and double-bumps has survived, even though it has slightly disintegrated (see Fig. 5.24). More precisely one fold (at $v_0 \approx -0.66$) has completely disintegrated and instead a large family of travelling localised states appeared, that do not correspond to single- and double-bumps as we have seen them before. In that parameter region the background of the localised bumps, which was mostly flat for all described states so far, is now unstable towards localised states. This is best explained by looking at the actual density profile of the states in question. In Fig. 5.25 for example, one can still recognize the main single-bump in the middle, but around it various smaller single- and double-bumps have formed. That state was found for $\overline{u} = -0.6703$ and hence not too far inside the chaotic structure seen in Fig. 5.24. If we take even higher values of $\overline{u}$ as for the exemplary state of Fig. 5.26, there is not even a main bump recognizable. Instead it looks like a random collection of localised single- and double-bumps. The numerous ways how these bumps could be arranged explains the complicated structure in Fig. 5.24.

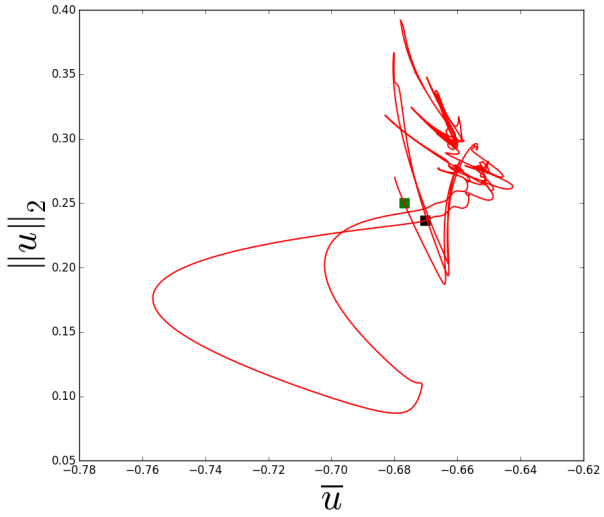

Figure 5.24: Bifurcation diagram of travelling single- and double-bumps as a function of $\overline{u}$ for $v_0 = 0.50$. The green square marks the bump-like structure in Fig. 5.25 and the black square the bump-like structure in Fig. 5.26.

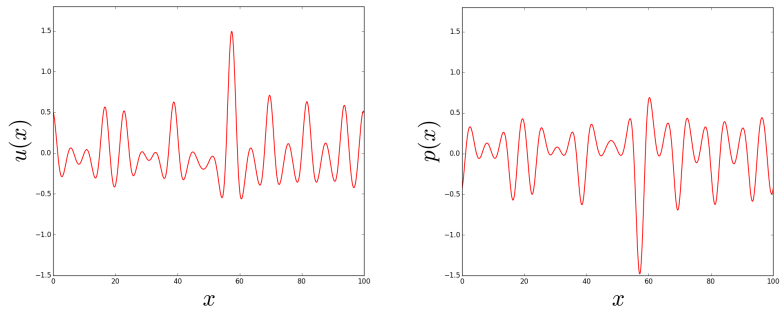

Figure 5.25: Density and polarization profile, $u(x)$ and $p(x)$ respectively, of travelling triple-bumps for $\overline{u} = -0.6703$ and $v_0 = 0.5$ with a velocity of $v = -0.4752$.

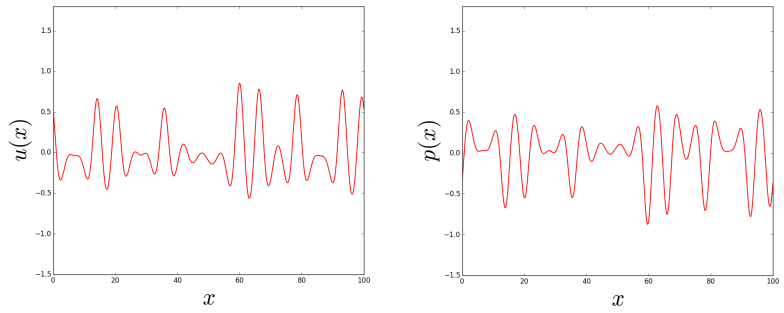

Figure 5.26: Density and polarization profile, $u(x)$ and $p(x)$ respectively, of travelling triple-bumps for $\overline{u} = -0.6769$ and $v_0 = 0.5$ with a velocity of $v = -0.4752$.

5.3 Fold continuation

5.3.1 Resting localised states

Finally, we turn to the continuation of the folds with respect to v_0 and $\overline{u}$ and start with that of all resting localised states. As one can see in Fig. 5.27 all have a closed structure except for two, the double- and triple-bumps, which run against the periodic state which is depicted in cyan. It is also interesting to note how the highest bump, the resting 15-tuple bump has a completely different form compared to the other fold continuations. The reason behind this is, that it depends on v_0 to which periodic state the localised states snake up to. For the PFC model ($v_0 = 0$) for example, the snaking ends in a periodic 15-tuple bump (see sec. 3.2.2). This is still the case until $v_0 \approx 0.12$, but for greater v_0 a periodic 16-tuple bump is approached. The cut is well visible in the bifurcation diagram of the fold continuation and we can deduce that there are four regions in total, where periodic states with various number of bumps are approached by the snaking process.

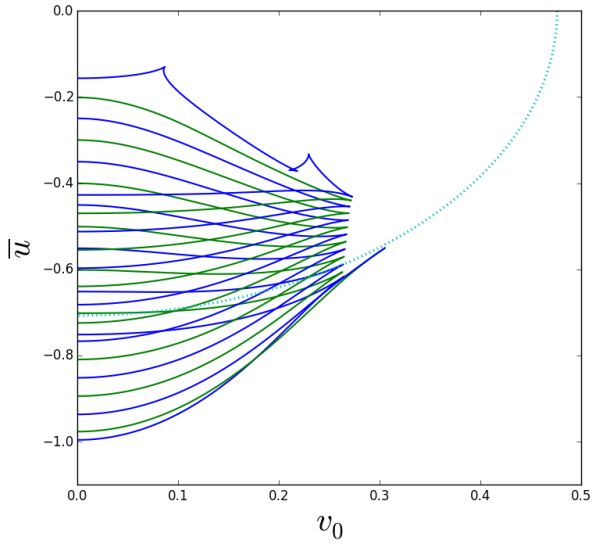

Figure 5.27: Loci of the saddle-node bifurcations on all resting localised states, from single to 15-tuple bumps. Resting localised states with an odd number of bumps are depicted blue, those with an even number of bumps green, while the periodic 17-tuple bump solution is depicted in cyan (dotted line).

Fig. 5.28 shows the fold continuation for a single structure, in this case the folds of single-bumps. Starting from low $\overline{u}$ the folds grow further apart, hence stretching the branch over a larger domain of v_0 as expected from previous observations. At $\overline{u} \approx -0.745$ two additional folds appear, which correspond to the connection of single- and triple-bumps as seen in sec. 5.1.4. The dashed lines correspond to the bifurcation diagrams at $\overline{u} = -0.775$ (Fig. 5.8), $\overline{u} = -0.75$ (Fig. 5.11) and $\overline{u} = -0.73$ (Fig. 5.14).

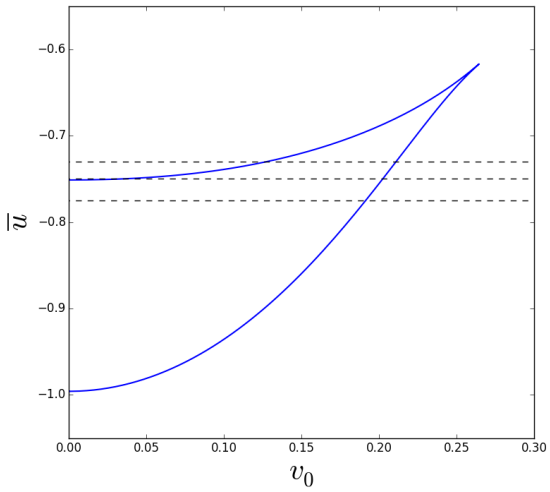

Figure 5.28: Loci of the saddle-node bifurcations on the resting localised single-bump (depicted in blue). The dashed lines are at -0.775, -0.75 and -0.73.

5.3.2 Single- and doublebumps

Fig. 5.29 contains the fold continuation for both single- and double-bumps. Several properties that we have observed during the continuation in either v_0 or $\overline{u}$ can be explained by looking at this diagram.
We begin by explaining how to connect the fold continuation to the bifurcation diagrams with only one continued parameter. Fig. 5.30 shows a close-up of the fold continuation of the left hand side with an additional dashed line at $\overline{u} = -0.75$. The crossings with that line denote the folds, that appear in the bifurcation diagram of $\overline{u} = -0.75$ (right hand side of Fig. 5.30). The very same procedure can be applied to the continuation in v_0. Fig. 5.31 shows the fold continuation with a dashed line at $v_0 = 0.17$ and indeed all crossings can be found as folds in the corresponding bifurcation diagram.
We therefore have exact knowledge about in which parameter region a given branch exists, since the fold continuation allows us to keep track of both the onset and disappearance of branches. Take the lower branch of single-bumps for example, Fig. 5.30 shows that the drift-pitchfork bifurcation dp_1 marks the onset of that branch in v_0 and 5.31 shows that the saddle-node bifurcations sd_1 and sd_3 mark onset and disappearance of the branch in $\overline{u}$. These information give us a region of existence in parameter space as plotted in Fig. 5.32.
Other effects observed in the previous sections are also well visible in the fold continuation. The divergence of single- and double-bump branch in Fig. 5.20 corresponds to the converging folds in the fold continuation (Fig. 5.29). Also all travelling localised states grow out of folds of resting localised states as had been observed for all parameters. The discontinued branch in Fig. 5.29 corresponds to the "background noise" discussed in sec. 5.2.3, where the disintegration of the fold has been discussed.

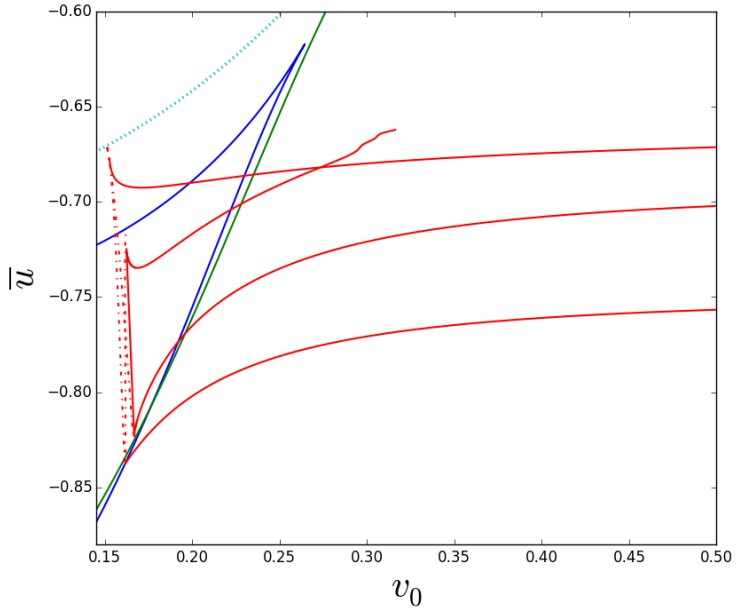

Figure 5.29: Loci of the saddle-node and drift-pitchfork bifurcations on all travelling single- and double-bumps. Resting single-bumps are depicted in blue, resting double-bumps in green, the resting periodic bump in cyan and the travelling bumps in red. Also saddle-node bifurcation have straight and drift-pitchfork bifurcation dotted lines.

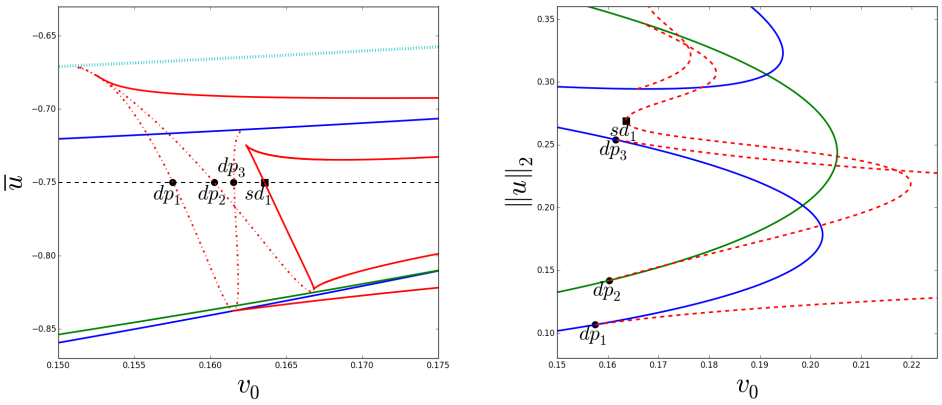

Figure 5.30: The left hand side shows a close-up of Fig. 5.29 with an additional dashed line at $\overline{u} = -0.75$. Crossings with a drift-pitchfork fold are labelled 'dp', while crossings with a saddle-node fold are labelled 'sd'. The right hand side shows the bifurcation diagram for $\overline{u} = -0.75$ with the corresponding position of the folds.

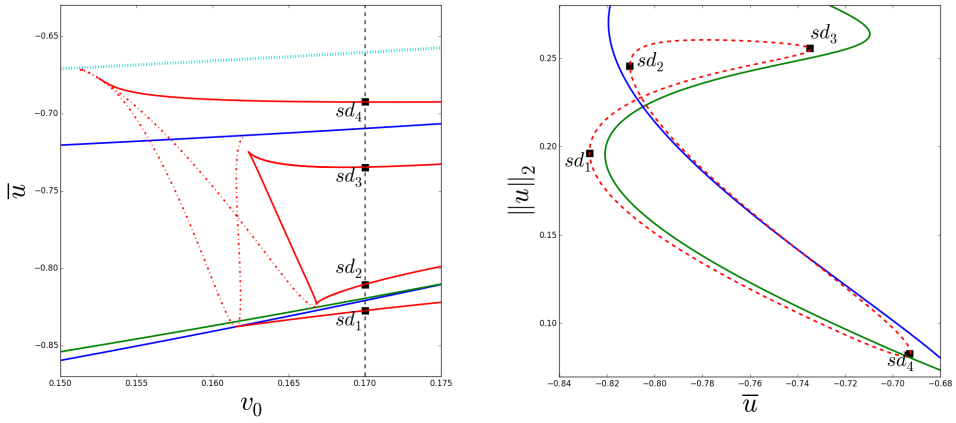

Figure 5.31: The left hand side shows a close-up of Fig. 5.29 with an additional dashed line at $v_0 = 0.17$. Crossings with a drift-pitchfork fold are labelled '*dp*', while crossings with a saddle-node fold are labelled '*sd*'. The right hand side shows the bifurcation diagram for $v_0 = 0.17$ with the corresponding position of the folds.

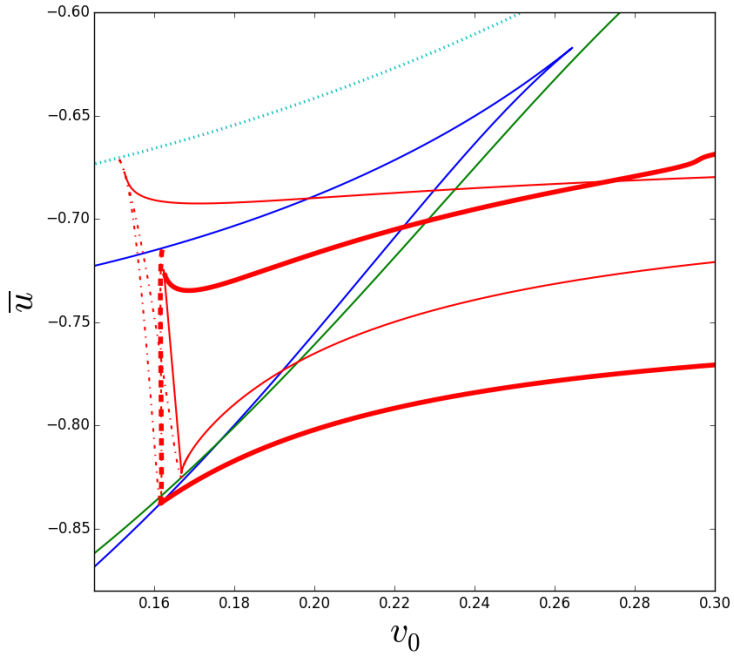

Figure 5.32: Loci of the saddle-node and drift-pitchfork bifurcations on all localised single- and double-bumps as in Fig. 5.29. The drift-pitchfork and saddle-node fold lines of the upper branch of the single-bumps are plotted as heavy lines, to illustrate the region of existence of that particular bump-type.

5.3.3 Double- and triple-bumps

The results of the fold continuation for double- and triple-bumps are plotted in Fig. 5.33 and show that these bumps only exist on a bounded region of the parameter space. This matches our expectations, since only the single- and lower double-bump branches diverged.
The folds of the travelling states connect the folds of resting bumps with same parity, meaning that resting double- & quadruple-bumps and triple- & quintuple-bumps are connected. This in turn means that a localised state comes into existence at for example a triple-bump fold and then, as $\overline{u}$ rises, switches branches and vanishes into a quintuple-bump fold.
The curved form of the saddle-node bifurcations in Fig. 5.33 is responsible for the pinch-off bifurcation that we discussed in Sec. 5.1.6. A close-up with dashed lines at -0.73, -0.727, -0.724 and -0.721 (Fig. 5.34) makes clear why. For rising $\overline{u}$ two pinch-off bifurcations occur leading to an isolated region of double- and triple-bumps as could be seen in Fig. 5.17. In fact, the dashed lines in Fig. 5.34 correspond exactly to the values of $\overline{u}$ for the four figures in Fig. 5.17.

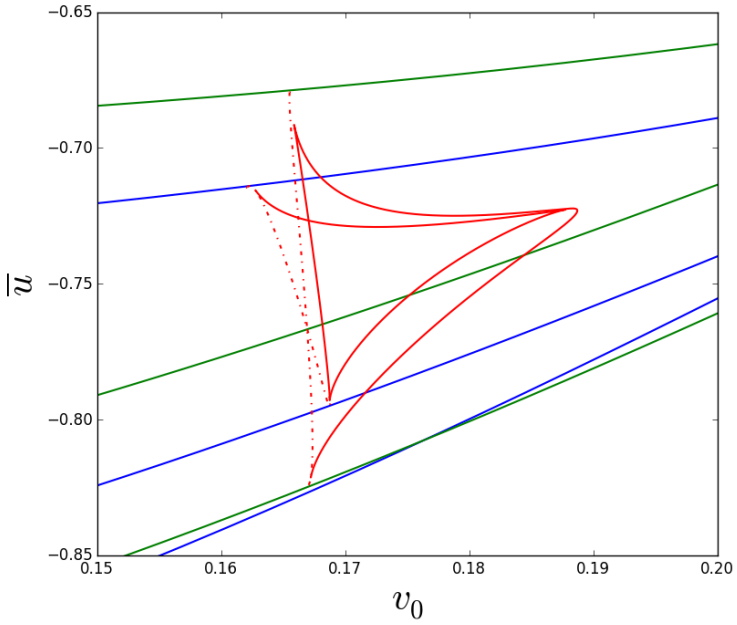

Figure 5.33: Loci of the saddle-node and drift-pitchfork bifurcations on all localised double- and triplebumps. Resting triple- and quadruple-bumps are depicted in blue, resting double-bumps and quadruple-bumps in green and the travelling bumps in red. Also saddle-node bifurcations have straight and drift-pitchfork bifurcations dotted lines.

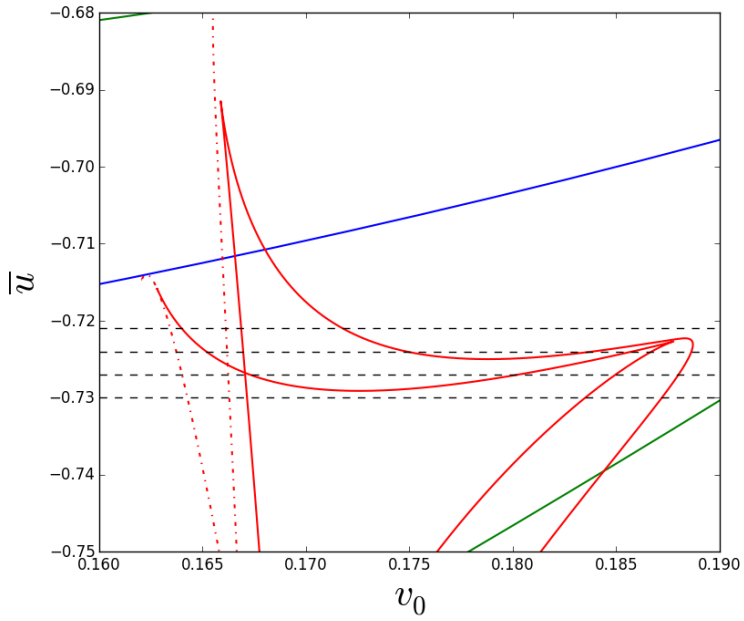

Figure 5.34: Close-up of Fig. 5.33 with additional dashed lines at -0.73, -0.727, -0.724 and -0.721.

5.3.4 All travelling localised states

Finally Fig. 5.35 shows the result of the fold continuation for travelling single-, double-, triple- and quadruple-bumps. It can be seen that the folds are all smoothly connected to each other.
The close-up in Fig. 5.36 describes the onset of the travelling double-bumps. The dashed lines at -0.827, -0.824, -0.821 and -0.817 indicate the values for $\overline{u}$, which were chosen already in Fig. 5.7 to describe the onset of double-bumps. It starts with two drift-pitchfork bifurcations and then, as $\overline{u}$ rises, gradually saddle-node bifurcations appear, which give the double-bump branch its distinctive structure (see Fig. 5.7). The very same process applies to triple- and quadruple-bumps, only the onset of single-bumps differs. The latter come into existence by two drift-pitchfork bifurcations, but there is only one saddle-node bifurcations to follow up. This is why the single-bumps do not have the curly structure of all the other bumps.
It is also interesting to note that the drift-pitchfork folds in Fig. 5.35 connect the onset and the disappearance of bumps with the same parity. The drift-pitchfork that marks the onset of double-bumps will eventually mark the disappearance of quadruple-bumps and likewise marks the same fold both the onset of single-bumps and the disappearance of triple-bumps.

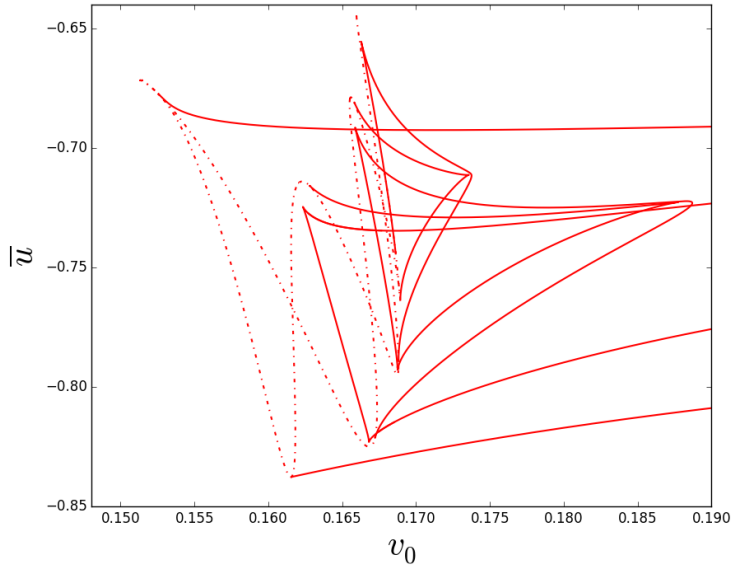

Figure 5.35: Loci of the saddle-node and drift-pitchfork bifurcations on travelling localised single-, double, triple, and quadruple-bumps. Saddle-node bifurcations have straight and drift-pitchfork bifurcations dotted lines.

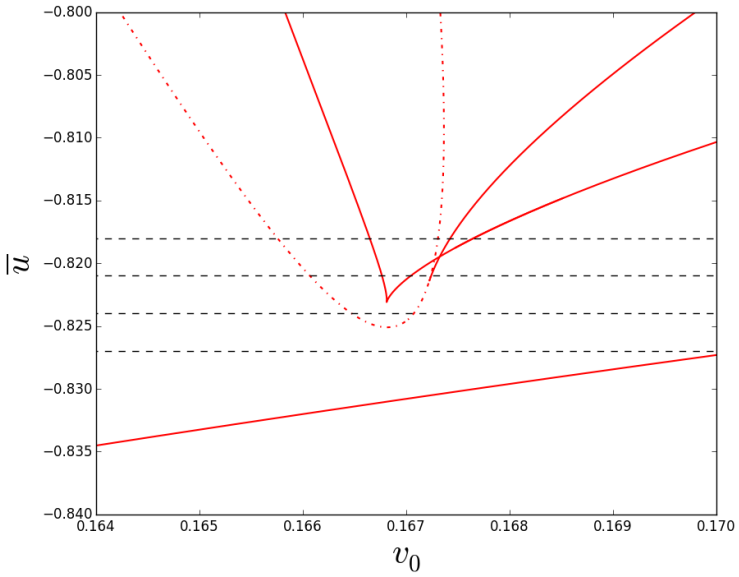

Figure 5.36: Close-up of Fig. 5.33 with additional dashed lines at -0.827, -0.824, -0.821 and -0.817.

5.3.5 All localised states

For the sake of completeness, we show the results of the fold continuation for all resting localised states, the periodic state and travelling localised states up to the quadruple-bump in one single diagram (Fig. 5.37).

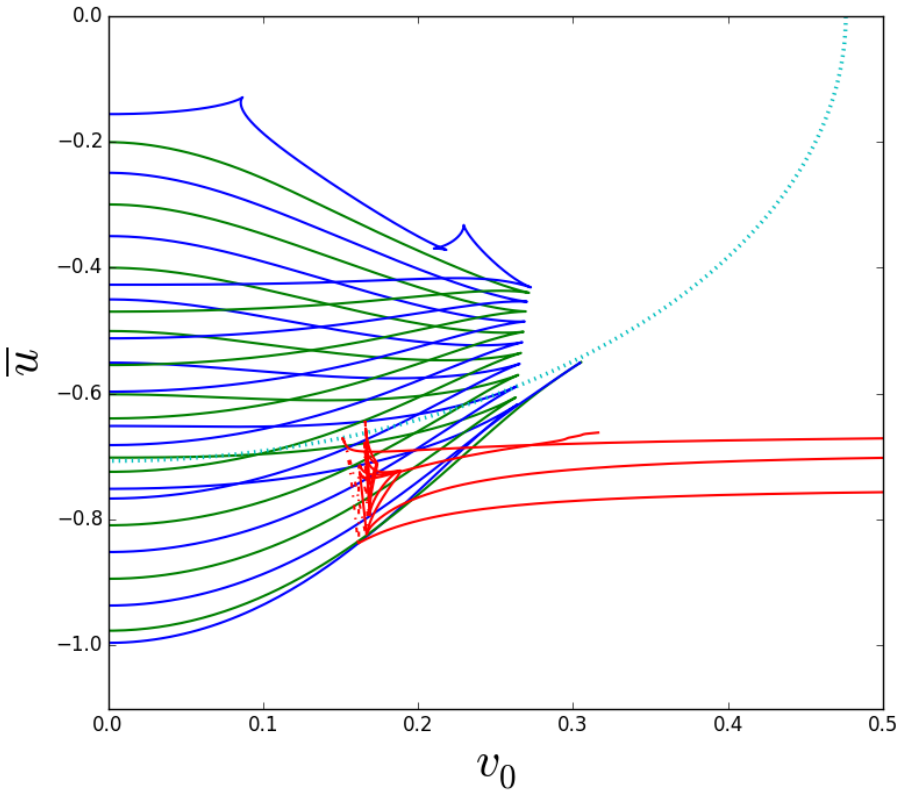

Figure 5.37: Loci of the saddle-node and drift-pitchfork bifurcations on all resting localised states, from single to 15-tuple bumps, and travelling localised states, up to quadruplebumps. Resting localised solutions with an odd number of bumps are depicted blue, those with an even number of bumps green, travelling localised states red, and the periodic 17-tuple bump solution is depicted in cyan.

6 Scattering

After obtaining an extensive description of the travelling localised states in the former section, we now test their scattering behaviour. Of special interest are single-bumps since their branches stretch over a large domain of v_0 (see Fig. 5.29) and numerical stability analysis has shown that their upper branch is linearly stable [28]. We thus dedicate the main section of this chapter to the scattering behaviour of single-bumps and then outline some basic scattering properties in the multi-bump region as well.

6.1 Scattering of single-bumps

Explicit solutions of the stable branch of single-bumps have been found with the continuation software AUTO07. Two of these solutions with identical v_0 and $\overline{u}$ but opposite velocity v are placed in a domain twice the size of the original domain (see Fig. 6.1). Time simulation of the order parameter equation (Eq. 4.5) is performed with a pseudospectral method and semi-implicit Euler time stepping (see Appendix for details).

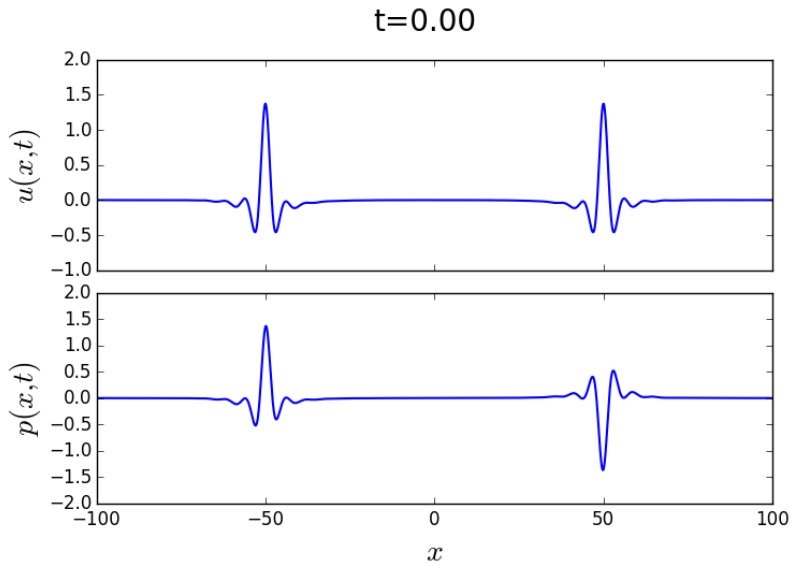

Figure 6.1: Initial position of the single-bumps, which are placed at $x = 50$ and $x = -50$, for $v_0 = 1.0$ and $\overline{u} = -0.73$. The bumps move with a velocity of $v = \pm 0.96$. The upper panel shows the density profile $u(x,t)$ and the lower panel the polarisation profile $p(x,t)$.

In the following we will explain a scattering process in detail and then analyse what makes a scattering event either elastic or inelastic. Finally a phase diagram in dependence of v_0 and $\overline{u}$ will be presented.

6.1.1 Scattering event

We start by explaining a generic scattering event in detail. In this thesis we make use of three different methods of describing scattering events. First, we can show the actual density profile $u(x,t)$ at different time steps, secondly we have the possibility of showing the L^2-Norm of u over time or, thirdly, we may present a space-time plot of $u(x,t)$. Depending on the context, one method may be more useful than the others.
The first scattering event we analyse is the collision of two single-bumps at $\overline{u} = -0.73$ and $v_0 = 1.0$. We highlight that process by explaining the collision for various time steps. While Fig. 6.2 shows the actual density profile at the given time step, Fig. 6.3 presents the L^2-Norm of u as a function of time and Fig. 6.4 shows the space-time plot during the scattering event.
We start at $t = 35$ where the two bumps are still in their original shape but are already very close to each other. As time evolves they both noticeably shrink as they further approach, as can be seen in the time steps at $t = 48$ and $t = 49$. Shortly after that at $t = 50$, exactly when their respective maxima are exactly on top of each other, they form one single bump of great size. This is also well visible in the L^2-Norm and the colour contour of the space-time plot. For $t = 52$ the size of the bump reduces considerably and at $t = 53$ two single peaks have reappeared. Those peaks are much smaller than the original peaks though. As time progresses to $t = 54$ they enhance a little, but only to shrink again at $t = 56$. At that time the bumps both start to regain their original shape, not their original size though since they are a lot smaller compared to before the collision. As the separation goes on the size rises steadily as seen at the pictures for $t = 64$ and $t = 70$, even though they are still well beyond their original size.
While the method of plotting the density profiles, as in Fig. 6.2, gives full information about the scattering process, it is also inconvenient. The L^2-Norm in Fig. 6.3 and the space-time plot in Fig. 6.4 are more compact, and hence a preferable method even though they have their shortcomings. The L^2-Norm gives a high resolution of the temporal evolution, but contains no information about the actual shape of $u(x,t)$. This method is therefore in the following only used, when the shape of the bumps after the collision is already known. The space-time plot gives in principle full information about the scattering process, but the collision itself cannot be studied as well as with the L^2-Norm. This method of presenting is hence preferable when dealing with collisions in the multi-bump region, where the outcome is unclear.

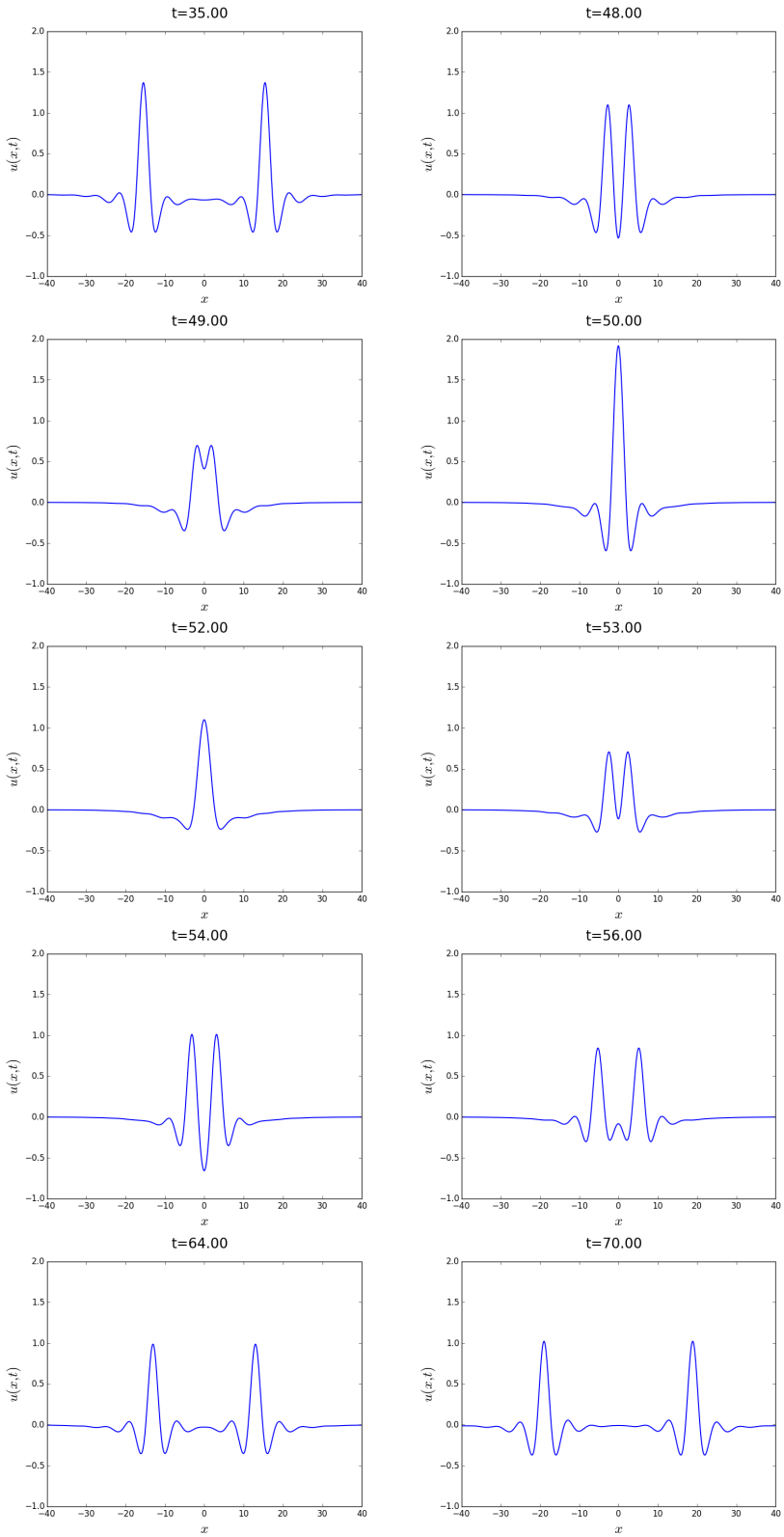

Figure 6.2: The density profile $u(x,t)$ of two singlebumps at $v_0 = 1.0$ and $\overline{u} = -0.73$ during a scattering event from $t = 35$ to $t = 70$.

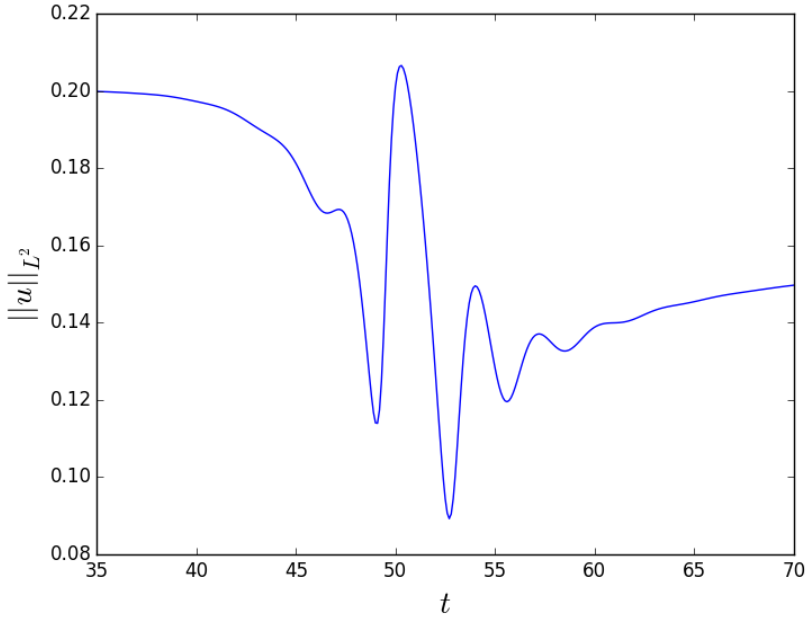

Figure 6.3: L^2-Norm of $u(x,t)$ during the scattering event from $t = 35$ to $t = 70$.

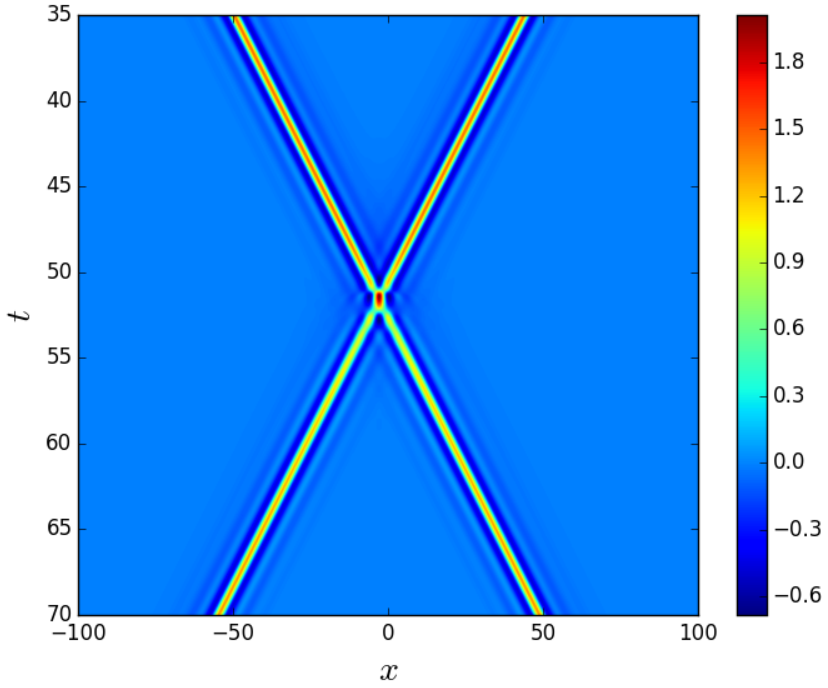

Figure 6.4: Space-time plot of $u(x,t)$ during the scattering event from $t = 35$ to $t = 70$.

6.1.2 Dependence on distance from unstable single-bump branch

It turns out that it is crucial whether the two single-bump branches are close to each other (see Fig. 6.5). By "close" we mean that their L^2-Norm is not too far apart. Since their shapes are almost identical and they effectively only differ in size, the L^2-Norm is a convenient measure to differentiate between the two branches. We have already seen in the previous section that the bumps shrink after a scattering event.
It is very important whether the outgoing single-bump is smaller than the lower single-bump solution, because the lower single-bump branch is an unstable solution which is in the middle of two stable solutions, namely the uniform state at $u = 0$ and the upper single-bump state. This implies, that when the bumps comes out of the collision smaller than the lower single-bump solution, it is going to decay towards the uniform state. If it comes out bigger than the lower single-bump branch solution it will run back to the upper single-bump solution. Therefore the scattering event is inelastic in the first case, and elastic in the second.
We will illustrate this process by looking at the specific scattering of two single-bumps at $v_0 = 1.0$ and varying $\overline{u}$. Fig. 6.5 shows the L^2-Norm of u for both single-bump branches as a function of $\overline{u}$. The solutions at $\overline{u} = -0.745, -0.740, -0.735, -0.730$ are highlighted by dashed lines. Apparently, the upper and lower branch solutions are the closest to each other for $\overline{u} = -0.745$ and are further apart for higher $\overline{u}$. We have performed four scattering experiments where the upper solutions with opposite velocity were scattered for each value of $\overline{u}$. The results are shown by the L^2-Norm in Fig. 6.6, where the L^2-Norm of the lower branch solutions are additionally indicated by a red line.
The single-bumps at $\overline{u} = -0.73$ come out of the collision with a size well above the lower single-bump solution, as can be seen in the top left corner of Fig. 6.6. Due to the periodic boundary condition the bumps keep on colliding, but the domain is large enough so that they have time to recover. The situation is already a little different for $\overline{u} = -0.735$. The bumps that come out of the collision are only just above the L^2-Norm of the lower single-bump solution. They do not have enough time to recover and multiple collisions keep on shrinking them up to the point where they are smaller than the lower single-bump solution (see Fig. 6.6). Therefore, they ultimately decay after surviving several collisions. The solutions at $\overline{u} = -0.74$ are even closer to each other and hence survive only one collision before decaying. Finally, for $\overline{u} = -0.745$ the scattering event is completely inelastic, since even the first collision leads to the immediate disintegration of both bumps.
The four exemplary scattering experiments provide a good overview over the scattering behaviour of single-bumps, the closeness of the lower single-bump branch is not the only criterium for an elastic collision. The actual velocity v of the bumps plays an important role too, as will be analysed in the next section.

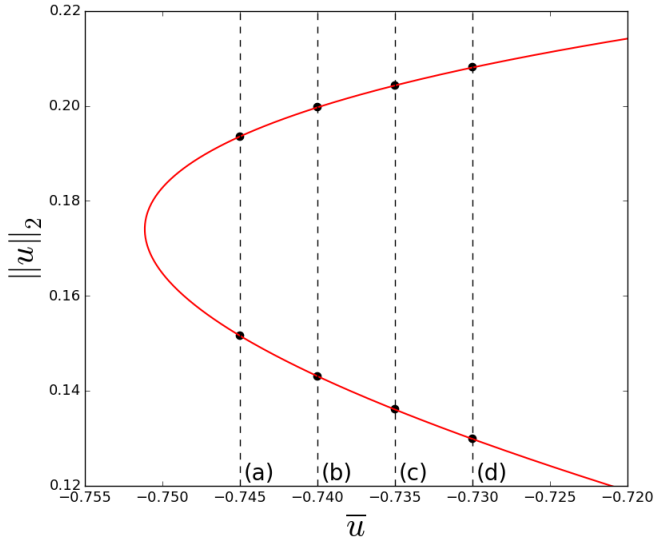

Figure 6.5: L^2-Norm of two branches of single-bumps (red) as a function of $\overline{u}$ at $v_0 = 1.0$. Markers indicate values of $\overline{u}$ where scattering experiments were performed, whose result are shown in Fig. 6.6.

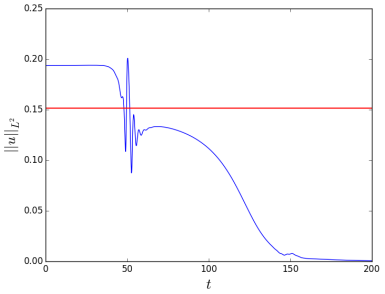

(a) $\overline{u} = -0.745$

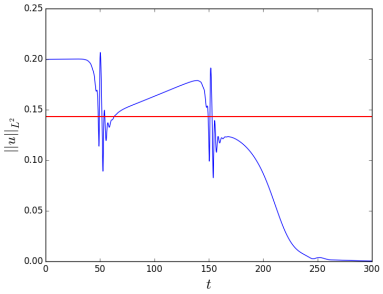

(b) $\overline{u} = -0.74$

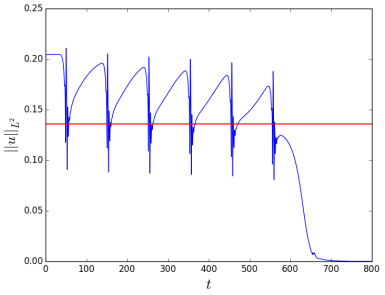

(c) $\overline{u} = -0.735$

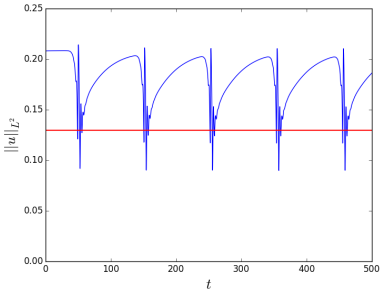

(d) $\overline{u} = -0.73$

Figure 6.6: L^2-Norm as a function of time for scattering events at $v_0 = 1.0$. The red lines correspond to the L^2-Norms of the lower single-bump branch solutions in Fig. 6.5, while the initial bumps were the upper single-bump branch solutions from Fig. 6.5.

6.1.3 Dependence on drift velocity

While the size of the lower single-bump is crucial, it is not the only entity influencing the outcome of a scattering experiment. The drift velocity v, which strongly correlates with the coupling parameter v_0 also has a large influence. There is the obvious influence in the sense that on a finite domain, the velocity is crucial in the recovering process of the bumps, as has been observed in the scattering experiments of the previous section (Fig. 6.6). There is another more direct influence independent of domain size.
We will illustrate this by performing two scattering experiments at $\overline{u} = -0.73$ and $v_0 = 0.4, 0.5$. Fig. 6.7 shows the L^2-Norm of the single-bumps in question. The two solutions are a little further apart for $v_0 = 0.4$ than they are for $v_0 = 0.5$. Even though the difference is not very large, one might expect from the previous section, that the collision at $v_0 = 0.4$ is more likely to be elastic than the collision at $v_0 = 0.5$. That turned out to not be the case, as can be seen in the L^2-Norm of the two scattering events (Fig. 6.8). In fact the opposite is the case, the scattering event at $v_0 = 0.5$ is elastic while the one at $v_0 = 0.4$ is not.
The reason behind that is that bumps with a lower velocity also spend more time in the immediate presence of each other. The collision process takes more time, has hence a larger influence and shrinks the size of the bumps even further.

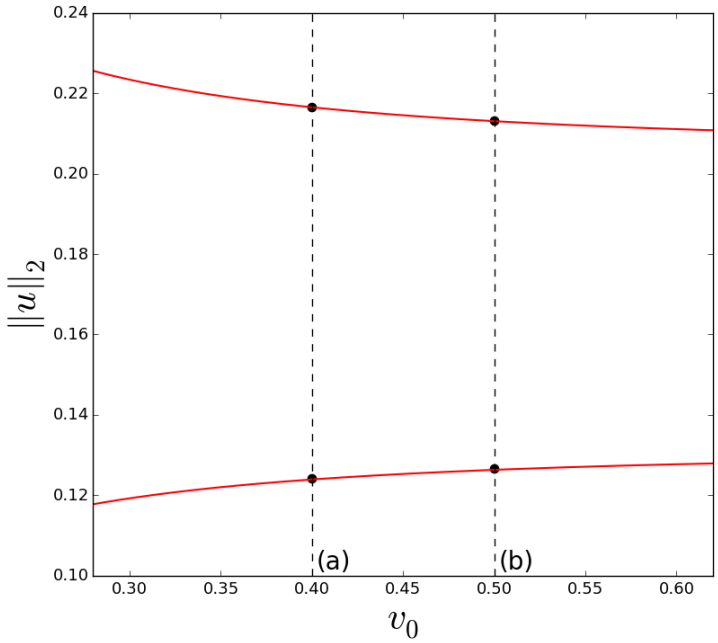

Figure 6.7: L^2-Norm of two branches of single-bumps (red) as a function of v_0 at $\overline{u} = -0.73$. Markers indicate values of $\overline{u}$ where scattering experiments were performed, whose result are shown in Fig. 6.8.

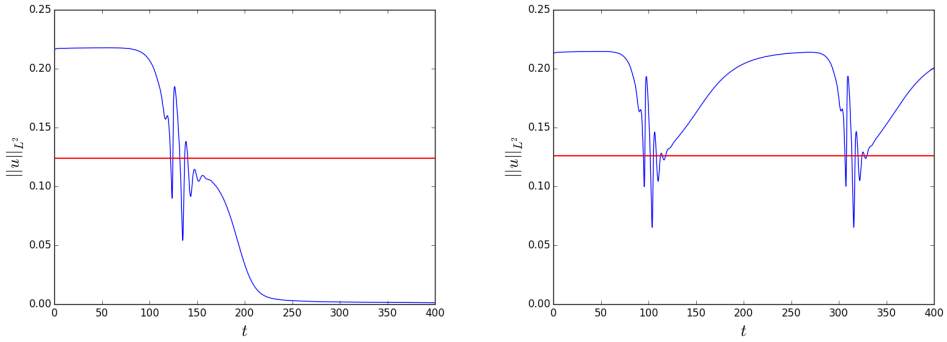

(a) $v_0 = 0.4$ **(b)** $v_0 = 0.5$

Figure 6.8: L^2-Norm as a function of time for scattering events at $\overline{u} = -0.73$. The red lines correspond to the L^2-Norms of the lower single-bump branch solutions in Fig. 6.7, while the initial bumps were the upper single-bump branch solutions from Fig. 6.7.

6.1.4 Phase diagram

After establishing the two criteria for an elastic collision, we can now create a phase diagram in dependence of v_0 and $\overline{u}$. We simulate scattering events from $v_0 = 0.2$ until $v_0 = 2.0$ in steps of 0.05 and from $\overline{u} = -0.77$ until $\overline{u} = -0.71$ in steps of 0.025. Single-bump solutions do not exist for all of these parameter values, but the fold continuation of section 5.3.2 gives full information about the region of existence. The borders of existence and information about the outcome of the experiments are plotted in the phase diagram (Fig. 6.9).
As long as the single-bump branches do not diverge ($\overline{u} \leq -0.75$), no fully elastic collisions are possible. The two branches of single-bumps are too close to each other, which can be seen for example in Fig. 5.11. As $\overline{u}$ exceeds -0.75, elastic collisions become possible, but still depend on v_0. That matches our expectations, since v_0 correlates to the velocity v and a high velocity is necessary to overcome the threshold.
The simulations are not continued above $\overline{u} = -0.71$, because bumps in that region develop strong "background noise" (see Fig. 5.24), which makes clean scattering events impossible. By "background noise", we mean that new bump-like structures emerge as for example in Fig. 6.10. We observe another very interesting and unexpected behaviour for very small v_0 (roughly $v_0 < 0.3$).
Instead of actually performing a collision the two bumps come to a halt when they get very close to each other, and then either merge into one single-bump or start to oscillate. The merging process occurs for lower values of $\overline{u}$, while the oscillations starts at $\overline{u} \approx -0.73$. The region coincides with the region of existence of travelling multi-bump states and the scattering behaviour in that region is studied in more detail in the next section.

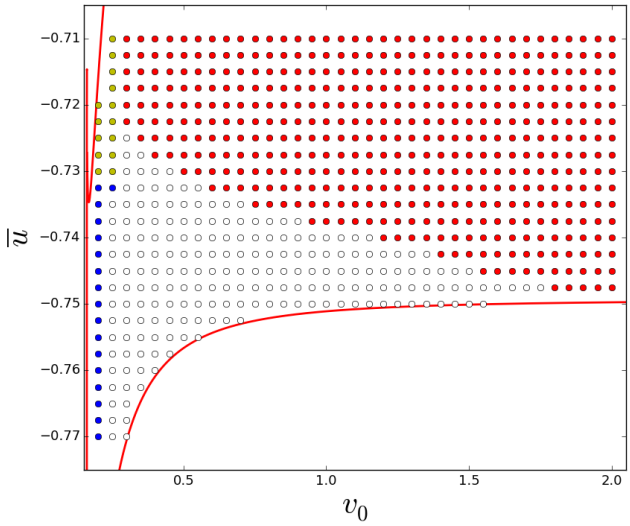

Figure 6.9: Phase diagram of scattering events for v_0 and $\overline{u}$. The red lines are obtained by fold continuation (see Fig. 5.29) and mark the region of existence of single-bumps. Red circles indicate an elastic collision, white circles an inelastic collision where the bumps decay, blue circles an inelastic collision where the bumps merge to one single-bump and yellow circles an inelastic collision where the bumps merge into an oscillating bump.

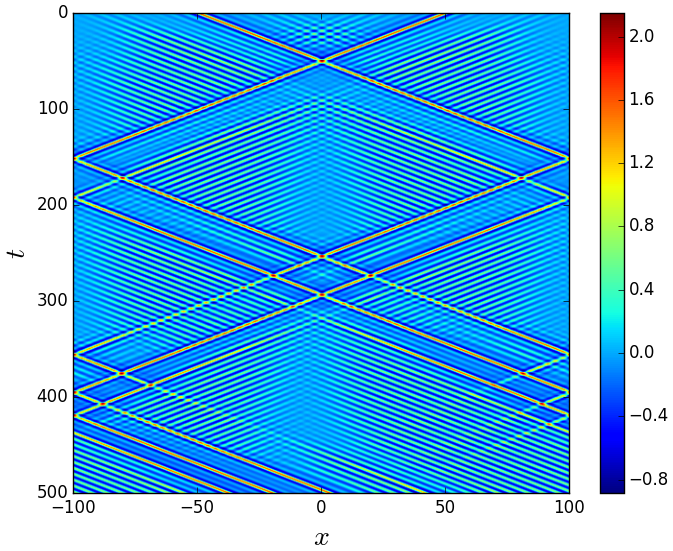

Figure 6.10: Space-time plot of two scattering single-bumps at $v_0 = 1.0$ and $\overline{u} = -0.66$.

6.2 Scattering in the multi-bump region

Scattering events of single-bumps are inelastic for small v_0 (see Fig. 6.9), which coincides with the presence of numerous travelling multi-bump states (see Fig. 5.35). Qualitatively, two kinds of behaviour have been observed in that region. Either the bumps merged to one single single-bump or the bumps merged and immediately started oscillating. Both cases are described in the following sections.

6.2.1 Merging bumps

Merging of two colliding bumps occurs only when two bumps approach each other with very small velocities ($v \ll 1$). As they approach they seem to come at rest and blend into a resting double-bump, as can be seen for example at $t \approx 400$ in Fig. 6.11. That resting period turned out to be rather short-lived though, as one of the peaks eventually decreases in size and the other peak starts travelling as a single bump, with the same velocity it had initially (Fig. 6.11). Merging dominates for small v_0 and low $\overline{u}$. That is also exactly the region where only few of the multi-bump states exist (see Fig. 5.35). For small v_0 but higher $\overline{u}$ the bumps usually do not merge, but start oscillating which is the topic of the next section.

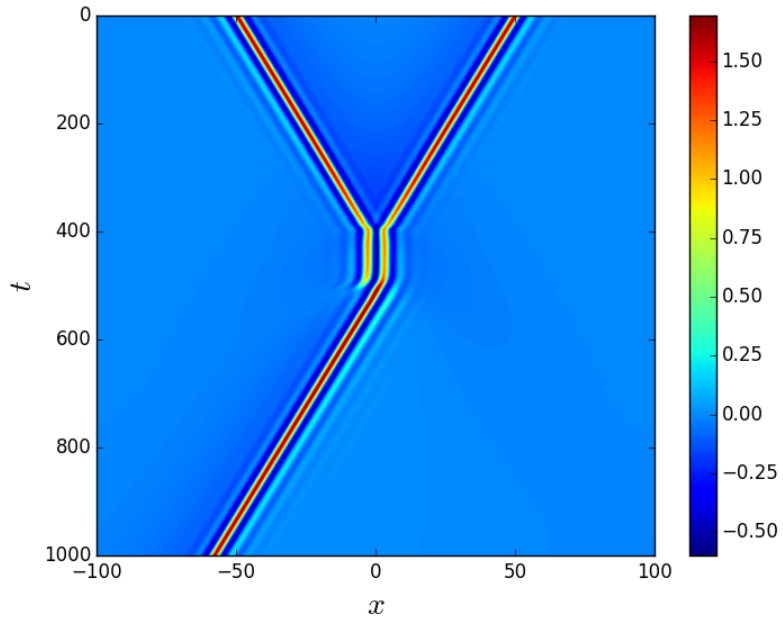

Figure 6.11: Space-time plot of two scattering singlebumps at $v_0 = 0.2$ and $\overline{u} = -0.75$, which merge at $t \approx 500$ into one travelling singlebump after appearing to rest for a short time before.

6.2.2 Oscillating bumps

For high average densities (roughly $\overline{u} > -0.74$) and low velocities ($v_0 < 0.3$), scattering events result in travelling oscillating states as for example the oscillating quintuple-bump shown in Fig. 6.12, 6.13 and 6.14. It should be noted that oscillating bumps are not limited to scattering events, but instead may appear in these parameter regions as well when bumps were just slightly perturbed, without any scattering.
However we discuss the oscillating bumps in the context of scattering and exemplary on the oscillating quintuple-bump that emerged from a scattering event of two single-bumps at $v_0 = 0.2$ and $\overline{u} = -0.73$. The space-time plot in Fig. 6.14 shows that the bumps initially behave like in the merging process, i.e. they approach each other and then seemingly come to rest as double-bump at $t \approx 400$. In contrast to the merging process none of the bumps decays, but they start moving in the same direction with the same velocity and start oscillating shortly afterwards. As time evolves the bump grows, new peaks arise and an oscillating double-bump finally ends up as oscillating quintuple-bump. The L^2-Norm of the scattering event in Fig. 6.13 shows clearly that the bump converges to a constant periodicity after a long time. The velocity of the resulting oscillating bump is also noticeably smaller than that of the initial single-bumps. Numerical simulations shows that for fixed parameters $v_0 = 0.2$ and $\overline{u} = -0.73$ the resulting oscillating bump does not depend on the initial setting. Scattering of double- or triple-bumps at the same parameter values also produces the very same oscillating quintuple-bump of Fig. 6.14.
For other values of v_0 and $\overline{u}$ the shape of the resulting oscillating bump varies, as we could also observe oscillating triple- and quadruple-bumps. It seems that the travelling stationary states undergo a Hopf-Bifurcation in this parameter region, which seemingly results in a variety of oscillating multi-bump branches.

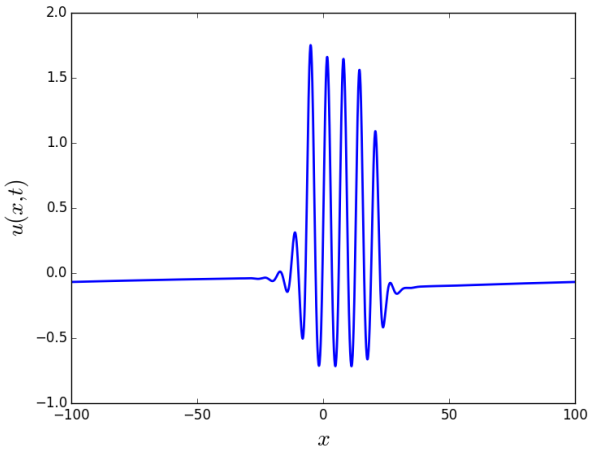

Figure 6.12: Density profile $u(x,t)$ of the oscillating quintuple-bump at $t = 100000$.

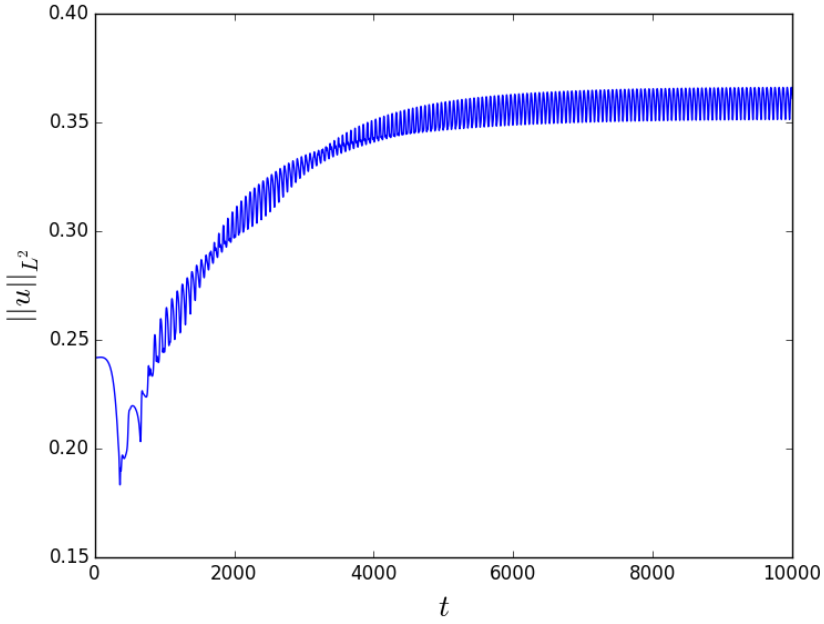

Figure 6.13: L^2-Norm of u of a scattering event at $v_0 = 0.2$ and $\overline{u} = -0.73$, that converges into an oscillating quintuple-bump.

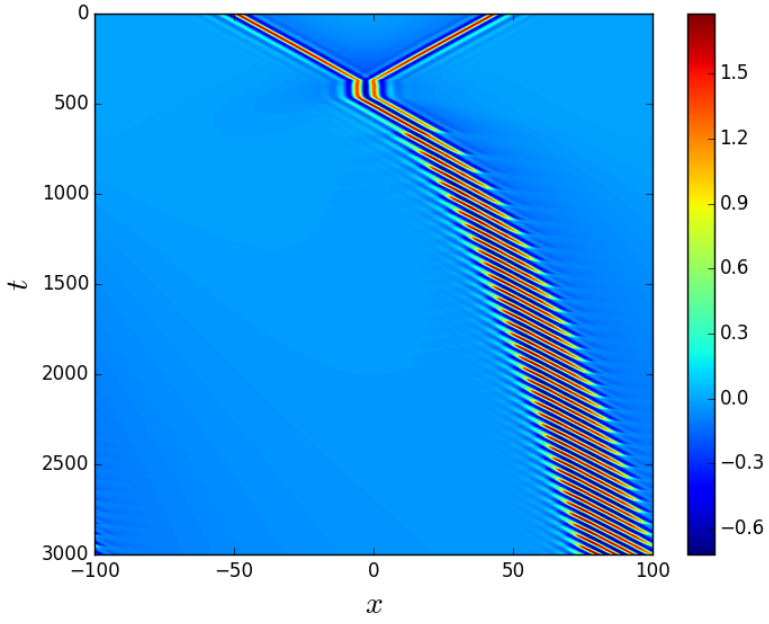

Figure 6.14: Space-time plot of $u(x,t)$ of a scattering event $v_0 = 0.2$ and $\overline{u} = -0.73$, that converges into an oscillating quintuplebump. Note that time simulation is only performed up to $t = 3000$.

7 Conclusion

The main goal of this thesis has been to describe the various localised states in the aPFC model and to investigate their scattering behaviour. We now shortly summarize main results and discuss their implications. Finally, we will suggest future extensions of the present work to further establish the aPFC model as a model for self-propelled particles, which exhibit crystallisation.
The SH equation, which is the topic of chapter 2, has been introduced as a simple model capable of describing the transition between a uniform state and crystalline states. It has been shown how the calculus of variation can be applied, outlining the great importance of steady states. In particular, it has been shown that travelling or oscillating states are forbidden. Also, numerical tools and analytical techniques, which are crucial for the whole thesis, have been introduced and used to determine the bifurcation diagram of periodic and localised states.
Chapter 3 has presented a more realistic model for the phase transition from uniform to crystalline states. We invoked statistical physics to derive the PFC model, which resembles the SH equation but also includes mass conservation. Localised states are found for the PFC model as well, but differences to the SH equation like for example the tilted snaking were discussed.
As last level in the model hierarchy, the aPFC model has been presented in chapter 4. It was first proposed by Menzel and Löwen in order to describe self-propelled particles, which form crystalline states at high densities. Their approach combines the PFC model with a self-propulsion equation following Toner-Tu theory. Linear stability analysis has resulted in a phase diagram showing three states, namely the uniform state, resting crystals and travelling crystals. Furthermore, the drift-instability, which was first described by Ophaus et al., has been presented. Linear stability analysis and the solvability condition of the drift-instability provided us with the required knowledge to finally tackle the analysis of the numerous branches of localised states.
We have chosen the coupling parameter v_0 and the average density $\overline{u}$ as continuation parameters for our analysis of the localised states in chapter 5. After showing numerous bifurcation diagrams for each parameter, we have also performed fold continuations to deepen our understanding. The fold continuation has provided us with further insight into the bifurcation behaviour of the localised states. In particular, this has allowed us to classify the region of existence for a given localised state, i.e. we can now name the precise parameter regions in v_0 and $\overline{u}$ for which each state exists. Interesting bifurcation behaviour, like for example the numerous pinch-off bifurcations, or the dense gas of coherent bump-like structures at high average density have been by-products of our analysis.

Finally, in chapter 6 we have considered the scattering behaviour of localised states. Motivated by the previous chapter, we have chosen a stable branch of single-bumps to investigate scattering events with varying coupling parameter v_0 and average density $\overline{u}$. We have observed four qualitatively differing results of a scattering event, namely that both bumps decay towards the uniform state, that both bumps merge into one single-bump, that they undergo an elastic collision and that they become a single oscillating multi-bump. We have provided a phase diagram in v_0 and $\overline{u}$ for these different outcomes.
The aPFC model has turned out to exhibit several interesting features and hence there exist many issues that one might look into in the future. The most intriguing one is the Hopf-Bifurcation, that seems to occur as has been described in chapter 6. The numerical continuation tool AUTO07 is not able to track Hopf-Bifurcations for spatially extended systems, but analytical methods like weakly nonlinear analysis, which was introduced in chapter 2 for the SH equation, could be adopted. Keeping in mind that the bio-physical motivation has been to describe self-propelled particles, it could also be interesting to find an interaction potential for the scattering process. It could be tried to apply the aPFC model to model an actual physical system, like for example microswimmers. We have only considered the one-dimensional aPFC model, but one should extend the study to two or even three spatial dimensions in order to develop a realistic model of self-propelled particles.

8 Appendix

8.1 Numerical continuation with AUTO07

Throughout this thesis we have used the numerical continuation tool AUTO07, the most recent version of the software package AUTO. An early version has been introduced by Doedel in 1981 [13], and since then many contributors helped improving the software. AUTO is heavily used in the scientific community and several updated versions were published over the years, with AUTO07 being the most recent one [1].
The main purpose of AUTO is to perform continuations of solutions of ordinary differential equation

$$u'(t) = f(u(t), \lambda), \tag{8.1}$$

where u is the function in question and λ the parameters. AUTO07 provides us with a large toolbox and can be used to determine bifurcation diagrams and solutions of the function in question.

8.2 Numerical time simulation

The numerical time simulation of the scattering experiments was done with the pseudospectral method. The idea of the latter is to transform a partial differential equation into Fourier space and hence get rid of the spatial derivatives. The resulting equation contains only temporal derivatives and can therefore be treated like an ordinary differential equation with for example the Runge-Kutta method.
We now illustrate that process for the aPFC order parameter equation (Eq. 4.5) and as a first step simplify the equations to

$$\partial_t u(x,t) = \mathcal{L}_u[\partial_x]u(x,t) + (u(x,t) + \overline{u})^3 - v_0 \partial_x p(x,t) \tag{8.2}$$
$$\partial_t p(x,t) = \mathcal{L}_p[\partial_x]p(x,t) - v_0 \partial_x u(x,t) \tag{8.3}$$

by introducing the shorthand notations $\mathcal{L}_u$ and $\mathcal{L}_p$. Their explicit form can be found in Eq. (4.8). We proceed by transforming the equations in Fourier space and obtain

$$\partial_t \tilde{u}(k,t) = \mathcal{L}_u[ik]\tilde{u}(k,t) + \mathcal{F}\left((\mathcal{F}^{-1}[\tilde{u}(k,t)] + \overline{u})^3\right) - ikv_0\tilde{p}(k,t) \tag{8.4}$$
$$\partial_t \tilde{p}(k,t) = \mathcal{L}_p[ik]\tilde{p}(k,t) - ikv_0\tilde{u}(k,t). \tag{8.5}$$

Note that we have indeed eliminated all spatial derivatives and can proceed by treating them like ordinary differential equations. In this case we chose the semi-explicit Euler method for time stepping.

Bibliography

[1] Auto-07p: Continuation and bifurcation software for ordinary differential equations. `http://www.macs.hw.ac.uk/~gabriel/auto07/auto.html`. [Online; accessed 08-October-2017].

[2] Münsteranian torturials on continuation. `https://www.uni-muenster.de/CeNoS/Lehre/Tutorials/auto.html`. [Online; accessed 05-October-2017].

[3] The nobel prize in chemistry 1998. `https://www.nobelprize.org/nobel_prizes/chemistry/laureates/1998/`. [Online; accessed 27-September-2017].

[4] J. R. Baylis, J. H. Yeon, M. H. Thomson, A. Kazerooni, X. Wang, A. E. St. John, E. B. Lim, D. Chien, A. Lee, J. Q. Zhang, J. M. Piret, L. S. Machan, T. F. Burke, N. J. White, and C. J. Kastrup. Self-propelled particles that transport cargo through flowing blood and halt hemorrhage. *Sci. Adv.*, 1, 2015.

[5] J. Bewersdorff. *Algebra für Einsteiger: Von der Gleichungsauflösung zur Galois-Theorie*. Vieweg Studium. Vieweg+Teubner Verlag, 2009.

[6] U. Bortolozzo, M. G. Clerc, and S. Residori. Solitary localized structures in a liquid crystal light-valve experiment. *New J. Phys.*, 11:093037, 2009.

[7] J. Burke and E. Knobloch. Localized states in the generalized Swift-Hohenberg equation. *Phys. Rev. E*, 73:056211, 2006.

[8] J. Burke and E. Knobloch. Snakes and ladders: Localized states in the Swift–Hohenberg equation. *Phys. Lett. A*, 6:681 – 688, 2007.

[9] A. I. Chervanyov, H. Gomez, and U. Thiele. Effect of the orientational relaxation on the collective motion of patterns formed by self-propelled particles. *EPL*, 115:68001, 2016.

[10] M. C. Cross and P. C. Hohenberg. Pattern formation outside of equilibrium. *Rev. Mod. Phys.*, 65:851–1112, 1993.

[11] B. Dacorogna. *Introduction to the Calculus of Variations*. EBL-Schweitzer. Imperial College Press, 2004.

[12] F. J. de Urries and J. Julve. Ostrogradski formalism for higher-derivative scalar field theories. *J. Phys. A*, 31:6949, 1998.

[13] E. Doedel. On the numerical analysis of dynamical systems, 1981.

[14] K. Drescher, J. Dunkel, L. H. Cisneros, S. Ganguly, and R. E. Goldstein. Fluid dynamics and noise in bacterial cell–cell and cell–surface scattering. *Proc. Natl. Acad. Sci.*, 108:10940–10945, 2011.

[15] K. R. Elder, M. Katakowski, M. Haataja, and M. Grant. Modeling elasticity in crystal growth. *Phys. Rev. Lett.*, 88:245701, 2002.

[16] H. Emmerich, H. Löwen, R. Wittkowski, T. Gruhn, G. I. Tóth, G. Tegze, and L. Gránásy. Phase-field-crystal models for condensed matter dynamics on atomic length and diffusive time scales: an overview. *Adv. Phys.*, 61:665–743, 2012.

[17] L. Evans. *Partial Differential Equations*. Graduate studies in mathematics. American Mathematical Society, 2010.

[18] H. Goldstein, C. Poole, and J. Safko. *Classical Mechanics*. Addison Wesley, 2002.

[19] J.-P. Hansen and I. R. McDonald. Chapter 3 - static properties of liquids: Thermodynamics and structure. In J.-P. Hansen, , and I. R. McDonald, editors, *Theory of Simple Liquids (Third Edition)*, pages 46 – 77. Academic Press, Burlington, third edition edition, 2006.

[20] G. Jeanmairet, N. Levy, M. Levesque, and D. Borgis. Introduction to classical density functional theory by a computational experiment. *J. Chem. Educ.*, 91:2112–2115, 2014.

[21] R. Kapral and K. Showalter. *Chemical Waves and Patterns*. Understanding Chemical Reactivity. Springer Netherlands, 2012.

[22] A. Liehr. *Dissipative Solitons in Reaction Diffusion Systems: Mechanisms, Dynamics, Interaction*. Springer Series in Synergetics. Springer Berlin Heidelberg, 2013.

[23] M. C. Marchetti, J. F. Joanny, S. Ramaswamy, T. B. Liverpool, J. Prost, M. Rao, and R. A. Simha. Hydrodynamics of soft active matter. *Rev. Mod. Phys.*, 85:1143–1189, 2013.

[24] P. C. Matthews and S. M. Cox. Pattern formation with a conservation law. *Nonlinearity*, 13:1293, 2000.

[25] A. M. Menzel and H. Löwen. Traveling and resting crystals in active systems. *Phys. Rev. Lett.*, 110:055702, 2013.

[26] A. M. Menzel, T. Ohta, and H. Löwen. Active crystals and their stability. *Phys. Rev. E*, 89:022301, 2014.

[27] N. D. Mermin. Thermal properties of the inhomogeneous electron gas. *Phys. Rev.*, 137:A1441–A1443, 1965.

[28] L. Ophaus, S. Gurevich, and U. Thiele. (in preparation).

[29] W. F. Paxton, K. C. Kistler, C. C. Olmeda, A. Sen, S. K. St. Angelo, Y. Cao, T. E. Mallouk, P. E. Lammert, and V. H. Crespi. Catalytic nanomotors: Autonomous movement of striped nanorods. *J. Am. Chem. Soc.*, 126:13424–13431, 2004.

[30] L. Pismen. Inertial effects in long-scale thermal convection. *Phys. Lett. A*, 116:241 – 244, 1986.

[31] T. V. Ramakrishnan and M. Yussouff. First-principles order-parameter theory of freezing. *Phys. Rev. B*, 19:2775–2794, 1979.

[32] R. Richter and I. V. Barashenkov. Two-dimensional solitons on the surface of magnetic fluids. *Phys. Rev. Lett.*, 94:184503, 2005.

[33] I. Theurkauff, C. Cottin-Bizonne, J. Palacci, C. Ybert, and L. Bocquet. Dynamic clustering in active colloidal suspensions with chemical signaling. *Phys. Rev. Lett.*, 108:268303, 2012.

[34] U. Thiele, A. J. Archer, M. J. Robbins, H. Gomez, and E. Knobloch. Localized states in the conserved Swift-Hohenberg equation with cubic nonlinearity. *Phys. Rev. E*, 87:042915, 2013.

[35] J. Toner and Y. Tu. Flocks, herds, and schools: A quantitative theory of flocking. *Phys. Rev. E*, 58:4828–4858, 1998.

[36] S. van Teeffelen, R. Backofen, A. Voigt, and H. Löwen. Derivation of the phase-field-crystal model for colloidal solidification. *Phys. Rev. E*, 79:051404, 2009.

Acknowledgements

Finally, I want to thank the following persons who contributed during the last year with their support, explanations and advices:

- Prof. Dr. Uwe Thiele, for providing me with the topic, advising my thesis and weekly discussions throughout the whole year. I am especially thankful for the excessive feedback during the writing process.
- Dr. Svetlana Gurevich, for being the second reader of my thesis and many fruitful discussions.
- Lukas Ophaus, for many fruitful discussions and proofreading my thesis.
- All members of AG Thiele, especially Fenna Stegemerten, Timmy Ly and Tobias Frohoff-Hülsmann, for pleasant lunchtimes, an excellent working atmosphere and many fruitful discussions.

Declaration of Academic Integrity

I hereby confirm that this thesis on *Scattering of localized states in the active phase field crystal (aPFC) model* is solely my own work and that I have used no sources or aids other than the ones stated. All passages in my thesis for which other sources, including electronic media, have been used, be it direct quotes or content references, have been acknowledged as such and the sources cited.

(date and signature of student)

I agree to have my thesis checked in order to rule out potential similarities with other works and to have my thesis stored in a database for this purpose.

(date and signature of student)